COHERENT MANIPULATIONS OF THE RUBIDIUM ATOM GROUND STATE

Thesis submitted in partial fulfillment of the requirement for the degree of master of science in the Faculty of Natural Sciences

Submitted by: **Amir Waxman**

Advisor: **Dr. Ron Folman**

Department of Physics

Faculty of Natural Sciences

Ben-Gurion University of the Negev

December 3, 2007

Abstract in hebrew

Abstract

In this thesis we study and analyze methods for coherent manipulation of rubidium atoms based on the interaction of radiation fields with the hyperfine levels of the ^{87}Rb ground state. Following the theoretical review, we describe our versatile laboratory system, capable of ^{87}Rb manipulation both by direct microwave radiation tuned to the ground-level hyperfine splitting and with a Raman laser system (two phase locked laser beams whose frequency difference is equal to the ground-level hyperfine splitting). We describe the atomic population oscillations (Rabi frequency of 0.2 - 3 KHz) induced by direct microwave radiation, including their dependence on the power and frequency of the microwave radiation, with and without constant magnetic field. Following that, we describe the setup of the Raman laser system, present our preliminary results, analyze the noise sources (i.e noncoherent processes) and check for the existence of coherent processes. We conclude with several proposals that may improve the performance of the Raman laser subsystem.

Acknowledgements

During the last tow years I had the pleasure of studying and working with a number of wonderful people who deserve thanks for their help and support during my research.

First of all I would like to thank my supervisor, Dr. Ron Folman, who provided me the opportunity to have fun playing with lasers and atoms in the lab. Despite his tight schedule, Ron always had the time to guide me through the fascinating world of atomic physics.

I am very grateful to Dr. David Grosswaser who recruited to help me in the experiment when I was desperate (i.e every other day). Thank you for your continuous readiness to spend time (which you usually do not have) helping me with the experimental setup.

I am also grateful to Dr. Plamen Petrov, a friend and a teacher. Thank you for being a walking encyclopedia of optics and electronics which is ready to answer all my ignorant questions.

I am thankfull to the B.E.C 1 guys, the Ph.D students Tal David and Ran Salem, who helped a lot while I was doing my first steps as an experimentalist. You were always ready to answer my trivial questions about experimental techniques, and "to go for coffee" whenever the lab became too small...

Many thanks to Dr. Yoni Yofe who never refused to discuss theoretical issues with me. Your explanations threw light on physical phenomena which I did not understand before.

I would like to acknowledge my "colleagues" - our Master students, the administrative stuff and the FAB people for the good time we shared, for friendly atmosphere you keep in the group, for your assistance and kindness.

And above all, thanks to Meny Givon. I find our work together both enjoyable and productive. With a lot of patience you guided me in my first steps in the lab. You were available at any time ready to have a serious discussion about everything (even if it was not physics). During the neverending period in which I wrote my thesis you gave me the professional and moral support I needed.

Thanks to my parents. Whatever success I have in my life is due to the beginnings which they gave me.

And finally, I would like to thank my beloved girlfriend, Liat, for being my strongest support and for your patience while my thoughts were wondering away to the physics world...

Contents

1 Introduction **7**

1.1 Motivation . . . 7

1.2 Thesis content . . . 9

2 Theory **10**

2.1 Two-level atom . . . 10

2.1.1 The Schrödinger equation for a two-state atom . . . 10

2.1.2 Constant interaction . . . 12

2.1.3 Rabi oscillations . . . 12

2.1.4 Microwave radiation . . . 14

2.1.5 The density matrix and the Bloch vector . . . 16

2.1.6 Rabi pulses and Ramsey fringes . . . 20

2.2 Stimulated Raman transitions . . . 23

2.2.1 The basics of Raman transitions . . . 23

2.2.2 Scattering rate . . . 25

2.2.3 Raman transitions in rubidium atoms . . . 26

2.2.4 The $\Delta m_F = 2$ problem . . . 27

2.2.5 An example: Coherent control of the atomic state . . . 30

3 The experimental system **31**

3.1 General structure of the system . . . 31

3.2 Lasers and laser locking . . . 33

3.2.1 Laser diodes . . . 33

3.2.2 External Cavity Diode Lasers (ECDL) . . . 35

3.2.3 Lasers in the experiment . . . 36

3.2.4 Polarization lock . . . 41

3.3 The atomic medium . . . 45

3.4 The detection system . . . 47

3.4.1 Thermal relaxation . . . 49

4 Rabi oscillations in the microwave field **51**

4.1 Experimental setup . . . 51

4.2 Results . . . 53

4.2.1 The dependency of Rabi oscillations on the field frequency . . . 54

4.2.2 The dependency of Rabi oscillations on the field power . . . 55

4.2.3 Oscillations in an external constant magnetic field . . . 57

4.3 Oscillation decay . . . 58

5 The Raman laser system **61**

5.1 Generation of the Raman beams . . . 61

5.1.1 Current modulation of a diode Laser . . . 62

5.1.2 Slave seeding (injection) . . . 64

5.2 Experimental setup . . . 67

5.3 Coherent and noncoherent results . . . 70

5.3.1 Rate equations . . . 71

5.3.2 The affect of the carrier . . . 72

5.3.3 The affect of non resonant excitation . . . 74

5.3.4 Coherent results . . . 76

6 Summary **78**

Appendices **79**

A The effect of the radiation phase on the Bloch vector's evolution **80**

B Double resonance spectroscopy **82**

Bibliography **83**

Chapter 1

Introduction

1.1 Motivation

The coherent control of a two-state quantum system has been the subject of many studies in recent years. Its applications range from the possibility of exploring fundamental aspects of quantum physics, to atomic clocks, magnetometers and quantum information processing. In our lab we are mainly interested in creating quantum superpositions for the measurement of decoherence.

A number of physical systems have been proposed to serve as the two-state system, among them superconducting circuits [Orl04], nuclear magnetic resonance [Van01] and trapped ions [Kin99]. The main advantages of neutral atoms as controllable quantum systems are their weak interaction with the environment and the rich variety of tools that can be used for the manipulation of both internal and external degrees of freedom.

Of special interest to us are alkali atoms. In these atoms, the hyperfine interaction between the electron spin and the nuclear spin splits the ground state into two levels whose frequency difference is in the order of several GHz. Those two levels can be treated as a two-state atom, since the energy difference between them and the first excited state corresponds to hundreds of THz. Alkali atoms, especially rubidium and cesium, are thus widely used to realize a two-state system.

In this thesis I describe coherent manipulations of the ^{87}Rb ground state.

The two-state atomic system may be represented by the Bloch sphere (Fig. 1.1). The

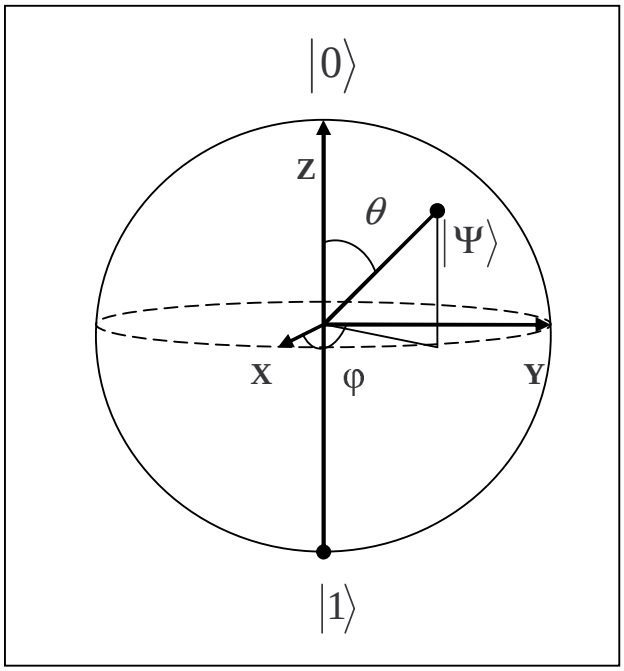

Figure 1.1: The Bloch Sphere

north and the south poles of that unit sphere represent the two pure states $|0\rangle$ and $|1\rangle$, corresponding to the ground and the excited states of the two-level atom (these states are often referred to as the computational qubit states). Any other point on the sphere represents a superposition state, namely,

$$|\Psi\rangle = \cos\frac{\theta}{2}|0\rangle + e^{i\phi}\sin\frac{\theta}{2}|1\rangle, \tag{1.1}$$

where we neglect the global phase, and ϕ and θ are the spherical coordinates. The evolution of the atomic state over time is expressed, in the Bloch picture, by the variation of ϕ and θ. Manipulation of the atomic state $|\Psi\rangle$ is achieved via interaction between the atom and some radiation field. The two hyperfine levels of the ^{87}Rb, serving as our two-state system, may be directly coupled by microwave radiation, but in order to address a small number of atoms (and even a single atom), we will prefer to use laser beams which can be tightly focused. The optical coupling is through a third intermediate level, in a stimulated Raman transition.

1.2 Thesis content

The organization of the thesis is as followed:

- Chapter 2: Theoretical concepts are discussed. In the first section we review the quantum-mechanical treatment of the two-level atom in the presence of external interaction. We also present the density-matrix formalism used to describe the behavior of ensembles of two-level atoms. In the second section we focus on the theory of the Raman transition. Besides the basic concepts, we discuss Raman transitions between Zeeman sublevels with $\Delta m_F = 2$, as those transitions are essential for the coherent manipulation of the magnetically trapped states of the ^{87}Rb atom.

- Chapter 3: Experimental concepts are reviewed. In the first section we discuss the physical properties of the lasers used in the experiment. We also demonstrate the laser locking system. In the next section, we discuss the properties of the atomic medium (^{87}Rb vapor cell) and describe the parameters affecting the interaction with the radiation field.

- Chapter 4: We describe the observed oscillations of the population in the ^{87}Rb ground state hyperfine levels, induced by direct microwave radiation. We also describe the behavior of the oscillations as a function of certain physical parameters.

- Chapter 5: The laser system built to induce Raman transitions in ^{87}Rb atoms is described in this chapter. The description of the generation of Raman beams is followed by presentation and analysis of preliminary results.

Chapter 2

Theory

2.1 Two-level atom

In this section we review some of the theory relevant to the atomic two-state system. We will mainly follow [Giv06], unless otherwise noted.

2.1.1 The Schrödinger equation for a two-state atom

In the absence of an external force, a two-state atom can be described using a time-independent Hamiltonian H_0. The system will then follow the eigenvalue equation

$$H_0\psi_n = E_n\psi_n \tag{2.1}$$

where the eigenvectors are orthogonal:

$$\langle\psi_m|\psi_n\rangle = \delta_{n,m}. \tag{2.2}$$

The atom's state vector $|\Psi(t)\rangle$ can be expressed as a superposition of the two orthogonal states:

$$|\Psi(t)\rangle = C_0(t)\psi_0 + C_1(t)\psi_1 \tag{2.3}$$

where the complex coefficient $C_n(t)$ is the projection $\langle\psi_n|\Psi(t)\rangle$ of the state vector $|\Psi(t)\rangle$ onto the basis vector ψ_n. Those two time-dependent functions are probability amplitudes, which means that the probability to find the atom in state n at time t is:

$$P_n(t) = |C_n(t)|^2 \equiv |\langle\psi_n|\Psi(t)\rangle|^2 \tag{2.4}$$

If we preform a measurement, at any time, we expect to find the atom in one of the two states, which means the probabilities should sum to unity; hence the condition

$$1 = |C_0|^2 + |C_1|^2. \tag{2.5}$$

If there is no interaction between the atom and its environment, the system is stationary, and the probability of finding the system in any one of the states is constant. It follows that the dependence of the amplitude C_n on time is only in the phase, and Eq. (2.3) can be written as:

$$\Psi(t) = e^{-i\frac{E_0 t}{\hbar}} C_0(0)\psi_0 + e^{-i\frac{E_1 t}{\hbar}} C_1(0)\psi_1 \tag{2.6}$$

Now we will add a time-dependent interaction, via the Hamiltonian

$$H(t) = H_0 + V(t). \tag{2.7}$$

To describe the coupling between the two states due to the interaction we have to calculate the matrix elements of $\hat{V}$ in the basis of H_0, namely

$$V_{nm} = \langle \psi_n | \hat{V} | \psi_m \rangle \tag{2.8}$$

where $V_{nm}(t) = V_{mn}(t)^*$ as $\hat{V}$ is Hermitian. The evolution of the state vector, $\Psi(t)$, is described by the time-dependent (TD) Schrödinger equation

$$\hbar \frac{\partial}{\partial t} \Psi(t) = -iH(t)\Psi(t). \tag{2.9}$$

Introducing (2.3) we get the equation for the amplitudes C_n:

$$i\hbar \frac{d}{dt} \begin{pmatrix} C_0(t) \\ C_1(t) \end{pmatrix} = \begin{pmatrix} E_0 + V_{00}(t) & V_{01}(t) \\ V_{10}(t) & E_1 + V_{11}(t) \end{pmatrix} \begin{pmatrix} C_0(t) \\ C_1(t) \end{pmatrix} \tag{2.10}$$

Once $V(t)$ and the initial conditions are specified, this equation provides the evolution of a two-state system subjected to an external interaction.

2.1.2 Constant interaction

Let us look at the simplest case, where $V(t)$ is turned on at $t = 0$, and remains unchanged, forming a step function of time. The matrix elements of $\hat{V}$ then read:

$$\begin{cases} t \leq 0 : V_{ij} = 0 (i, j = 0, 1) \\ t > 0 : V_{00} = \frac{\hbar}{2}(2\bar{\omega} - \omega_0) - E_0; V_{11} = \frac{\hbar}{2}(2\bar{\omega} + \omega_0) - E_1 \\ t > 0 : V_{10} = V_{01} = const. \equiv \frac{1}{2}\hbar\Omega \end{cases} \tag{2.11}$$

where $\hbar\omega_0$ is the energy difference between the two states and $\hbar\bar{\omega}$ is their average energy. Setting $\bar{\omega}$ to zero (by doing so we just change the zero point of the energy and not the energy difference between the states) and substituting (2.11) in the TD Schrödinger equation (2.10), we get

$$i\frac{d}{dt}\begin{pmatrix} C_0(t) \\ C_1(t) \end{pmatrix} = \frac{1}{2}\begin{pmatrix} -\omega_0 & \Omega \\ \Omega & +\omega_0 \end{pmatrix}\begin{pmatrix} C_0(t) \\ C_1(t) \end{pmatrix} \tag{2.12}$$

which implies

$$\frac{d^2}{dt^2}C_i = -\frac{1}{4}\tilde{\Omega}^2 C_i(t) \tag{2.13}$$

where $\tilde{\Omega}^2 = \Omega^2 + {\omega_0}^2$ and $i = 0, 1$. The solution of this equation with the initial conditions $C_0 = 1; C_1 = 0$ yields the probability to find the atom in state $|1\rangle$ at any time t:

$$P_1(t) = C_1(t)^2 = \frac{1}{2}(\Omega/\tilde{\Omega})^2[1 - \cos(\tilde{\Omega}t)] \tag{2.14}$$

This result predicts population oscillations of a two-state atom subjected to a constant interaction: The probability of finding the atom in any one of the states oscillates in time with the amplitude $\frac{1}{2}(\Omega/\tilde{\Omega})$. When the interaction is weak ($\Omega \ll \omega_0$), the amplitude approaches zero, and the oscillations are small. For strong interactions, the amplitude approaches 1/2, and the population moves completely from one state to the other.

2.1.3 Rabi oscillations

We will now check how a periodically changing interaction (such as that introduced by laser light), will affect our two-state system.

The interaction between the atom and the laser electric field $\hat{E}(t)$ is governed by the electric dipole interaction

$$\hat{V}_{dip} = -\mathbf{d} \cdot \mathbf{E} \tag{2.15}$$

where $\hat{\mathbf{d}}$ is the induced atomic dipole moment. The coupling strength of the interaction is characterized by the Rabi frequency [Sho90]

$$\Omega = -\frac{\mathbf{d} \cdot \mathbf{E}}{\hbar} = \frac{|\overrightarrow{d_{10}} \cdot \overrightarrow{\epsilon}|}{e a_0} \sqrt{\frac{8\pi e^2 {a_0}^2}{\hbar^2 c^2}} \sqrt{I} \tag{2.16}$$

where d_{10} is the dipole matrix element $\langle 0| \overrightarrow{d} |1\rangle$, $\overrightarrow{\epsilon}$ is the unit vector in the direction of the electric field produced by the laser, and I is the laser intensity. If we consider, for example, circularly polarized light, the matrix elements of $\hat{V}$ will be

$$\begin{cases} V_{00} = V_{11} = 0 \\ V_{01} = {V_{10}}^* = \frac{1}{2}|\hbar\Omega| e^{-i(\omega t + \varphi)} \end{cases} \tag{2.17}$$

Substituting (2.17) into the TD Schrödinger equation (2.9) and transforming to the rotating wave picture (i.e. to a reference frame that rotates at the laser frequency) we get the following equations for the probability amplitudes:

$$\frac{d}{dt} \begin{pmatrix} C_0(t) \\ C_1(t) \end{pmatrix} = -\frac{i}{2} \begin{pmatrix} -\delta & |\Omega| \\ |\Omega| & \delta \end{pmatrix} \begin{pmatrix} C_0(t) \\ C_1(t) \end{pmatrix} \tag{2.18}$$

where $\delta = \omega_0 - \omega$ is the detuning between the laser frequency and the resonant transition frequency ω_0. We can now solve this equation, with the initial condition $C_0(0) = 1$ (atom in the ground state) to get the probability of finding the atom in the excited state at any time t:

$$P_1(t) = C_1(t)^2 = \frac{1}{2} \frac{|\Omega|^2}{\bar{\Omega}^2} [1 - \cos(\bar{\Omega} t)] \tag{2.19}$$

This probability oscillates at the flopping frequency $\bar{\Omega} = \sqrt{|\Omega|^2 + \delta^2}$, which is dependent both on the laser intensity (expressed by the Rabi frequency) and frequency (expressed by the detuning). The amplitude of these oscillations, on the other hand, depends solely on the laser frequency. In the resonant case ($\omega = \omega_0$), the population alternates between complete concentration in state $|0\rangle$ and complete inversion to state $|1\rangle$. As we increase the detuning, the oscillations amplitude is attenuated. That is well demonstrated in Fig. 2.1.

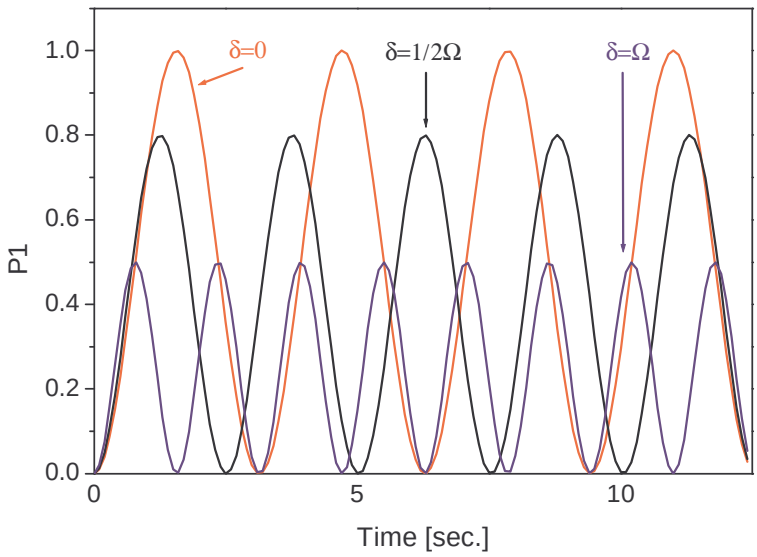

Figure 2.1: Rabi oscillations for different detunings ($\Omega = 2rad/sec.$). In the red plot $\delta = 0$, in the black plot $\delta = 1/2\Omega$, and in the blue plot $\delta = \Omega$

2.1.4 Microwave radiation

The hyperfine interaction splits the ground state of ^{87}Rb into two hyperfine levels $F = 1$ and $F = 2$. The hyperfine splitting is $\Delta_{HFS} = 2\pi{\cdot}6.834682610$ GHz (see the levels diagram of the ground and first excited state in Fig. 2.2).

Direct coupling of these levels, through one-photon transition is thus realized using microwave radiation. As both states have spherical symmetry (= the electric dipole is zero) this transition is governed by the magnetic dipole potential

$$V = (\mu_{\mathbf{L}} + \mu_{\mathbf{S}} + \mu_{\mathbf{I}}) \cdot \mathbf{B}. \tag{2.20}$$

The orbital magnetic moment originates from the valence electron moving around the nucleus. It is given by

$$\mu_{\mathbf{L}} = \frac{\mu_B}{\hbar} g_L \mathbf{L} \tag{2.21}$$

where $\mu_B = e\hbar/2m_e$ is the Bohr magneton. The magnetic dipole moments $\mu_{\mathbf{S}}$ and $\mu_{\mathbf{I}}$ (associated with the valence electron and the nucleus respectively) are proportional to the electronic spin angular momentum $\mathbf{S}$ and the nuclear spin angular momentum $\mathbf{I}$ via

$$\mu_{\mathbf{S}} = \frac{\mu_B}{\hbar} g_S \mathbf{S} \tag{2.22}$$

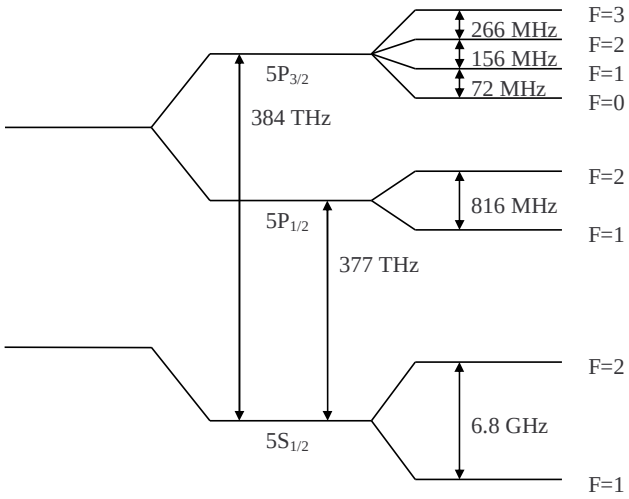

Figure 2.2: The fine structure and the hyperfine structure of the ground state and the first excited state in ^{87}Rb with some of the relevant energy differences.

$$\mu_{\mathbf{I}} = \frac{\mu_N}{\hbar} g_I \mathbf{I} \tag{2.23}$$

We will calculate the perturbation energy V (see Eq. 2.10) resulting from the interaction of the atom with the magnetic component of the microwave radiation. Let us consider, as the unperturbed system, a rubidium atom in a weak uniform and static magnetic field B_0 along the z-direction. The bias field B_0 defines an axis of quantization. As we choose the field to be very weak, the Zeeman splitting is relatively small, and we may still assume that the unperturbed Hamiltonian H_0 commutes with L^2, S^2, I^2, F^2 and F_z. We assume further that the magnetic field induced by a linearly polarized magnetic wave oscillates in the direction of the bias field, or

$$\mathbf{B} = \hat{\mathbf{z}} B_1 \cos(\omega t - \mathbf{R}_0 \cdot \mathbf{k}) \tag{2.24}$$

where $\mathbf{R}_0$ is the atom's center-of-mass point. As the ground state hyperfine levels are both s-states ($L = 0$), only the terms $\mu_{\mathbf{S}} \cdot \mathbf{B}$ and $\mu_{\mathbf{I}} \cdot \mathbf{B}$ contribute to the interaction energy:

$$V = \frac{B_1}{\hbar} (\mu_B g_S S_z + \mu_N g_I I_z) \cos(\omega t), \tag{2.25}$$

where we took $\mathbf{R}_0$ to zero for convenience.

The matrix elements of $\hat{V}$ are calculated between two Zeeman sublevels in the basis $\{I_z, S_z\}$.

Here we only detail the matrix element calculation for the clock transition ($m_F = 0 \rightarrow m'_F = 0$):

$$V_{12} = \langle F = 1, m_F = 0|V|F = 2, m_F = 0\rangle = \frac{B_1}{2\hbar}\cos(\omega t)\left[\langle\frac{1}{2}, -\frac{1}{2}| + \langle -\frac{1}{2}, \frac{1}{2}|\right] \times$$
$$\times(\mu_B g_S S_z + \mu_B g_I I_z) \times \left[|\frac{1}{2}, -\frac{1}{2}\rangle - | - \frac{1}{2}, \frac{1}{2}\rangle\right] = \frac{-B_1}{2}\cos(\omega t)(\mu_B g_S - \mu_B g_I). \quad (2.26)$$

For the other $\Delta m_F = 0$ transitions we get:

$$\langle 1, -1|V|2, -1\rangle = \langle 1, 1|V|2, 1\rangle = \frac{-\sqrt{3}B_1}{4}\cos(\omega t)(\mu_B g_S - \mu_B g_I). \quad (2.27)$$

Since we took the microwave field to be linearly polarized, the matrix element is zero for $\Delta m_F \neq 0$.

The next step is solving the rate equations derived from the Schrödinger equation (as was done in the previous section for the electric dipole interaction). The solution predicts our system, initially prepared in the ground state, will undergo oscillations between the two states at a rate determined by the generalized Rabi frequency (see Eq. 2.19). The Rabi frequency induced by the interaction is defined as a measure of the interaction strength, and therefore is proportional to the magnetic field B_1. For the clock transition, in particular, it reads

$$\Omega = \frac{-B_1}{2\hbar}(\mu_B g_S - \mu_B g_I). \quad (2.28)$$

The generalized Rabi frequency (also called the flopping frequency) induced by a microwave pulse at the frequency ω is

$$\bar{\Omega} = \sqrt{\Omega^2 + (\omega - \omega_0)^2}, \quad (2.29)$$

where ω_0 is the transition frequency.

2.1.5 The density matrix and the Bloch vector

The periodic probability oscillations discussed in the previous sections cannot be observed in a single atom. To notice these oscillations one needs to have an ensemble of two-level atoms. In the following we will develop the tools to deal with such an ensemble.

Let us assume that at time t=0 we can define an ensemble of two-state atoms through a set

of wave functions $\Psi_i(0)$, each representing a fraction p_i of the atoms in that ensemble. We can then define the density matrix, or the density operator,

$$\hat{\rho}(0) = \sum_i p_i |\Psi_i(0)\rangle\langle\Psi_i(0)|, \tag{2.30}$$

with $\sum p_i = 1$. The evolution of the density matrix in time is described by the Liouvile equation:

$$i\hbar\frac{\partial}{\partial t}\hat{\rho}(t) = [H, \hat{\rho}(t)] \tag{2.31}$$

and the expectation value of any operator $\hat{A}$ is given by

$$\langle\hat{A}\rangle = Tr(\hat{\rho}\hat{A}). \tag{2.32}$$

Let us now look at the density matrix in the basis defined by the basis vectors ψ_0 and ψ_1, corresponding to the ground and excited states of the unperturbed Hamiltonian H_0:

$$\hat{\rho} = \begin{pmatrix} \rho_{00} & \rho_{10} \\ \rho_{01} & \rho_{11} \end{pmatrix}. \tag{2.33}$$

The diagonal elements of that matrix are populations,

$$P_0 = \rho_{00}; P_1 = \rho_{11}, \tag{2.34}$$

therefore,

$$Tr(\hat{\rho}) = 1. \tag{2.35}$$

The variation of these elements over time indicates a transfer of population among the two basis states. The off-diagonal elements $\rho_{10} = {\rho_{01}}^*$, sometimes termed *coherences*, are related to the interaction between the two basis states. The variation of these elements over time, indicating a change in the coupling strength of the two states, is also referred to as a change in the coherence.

Let us assume the system is initially in one of the basis states, say the ground state. In the absence of interactions, the density matrix will take the form

$$\hat{\rho} = \begin{pmatrix} 1 & 0 \\ 0 & 0 \end{pmatrix}. \tag{2.36}$$

This matrix describes a pure state. More generally, a pure state will be some coherent superposition of the basis states. For example, the matrix

$$\hat{\rho} = \begin{pmatrix} 1/2 & i/2 \\ -i/2 & 1/2 \end{pmatrix} \tag{2.37}$$

also represents a pure state. In general, if the density matrix describes a pure state then

$$\hat{\rho}\hat{\rho} = \hat{\rho} \tag{2.38}$$

[Sho90] holds. Otherwise it describes a mixed state.

The two-state system can also be represented by the Bloch sphere (see Sect. 1.1). In that picture we can define the Bloch vector as the unit vector connecting the origin to a point (θ, ϕ) on the sphere. The Cartesian components of the Bloch vector are:

$$\hat{\nu}^B = (\nu_x, \nu_y, \nu_z) = (\sin\theta\cos\phi, \sin\theta\sin\phi, \cos\theta). \tag{2.39}$$

The density matrix for a two-level system can be written as [Mab01]

$$\hat{\rho} = \frac{1}{2}(1 + \nu^B \cdot \hat{\sigma}), \tag{2.40}$$

where $\hat{\sigma}$ denotes the Pauli matrices. Substituting (2.39) into (2.40) we get the density matrix elements expressed via Bloch vector components:

$$\hat{\rho} = \frac{1}{2}\begin{pmatrix} 1+\nu_z & \nu_x - i\nu_y \\ \nu_x + i\nu_y & 1-\nu_z \end{pmatrix}. \tag{2.41}$$

Using the above-mentioned properties of the density matrix, we can derive the following regarding the Bloch vector components: First, the component $\nu_z = \rho_{00} - \rho_{11}$ indicates population, ranging from 1 (the top point of the Bloch sphere) to -1 (the bottom point), while the components $\nu_x = \rho_{01} + \rho_{10}$ and $\nu_y = i(\rho_{10} - \rho_{01})$ indicate coherence between the states. Second, the Bloch vector will describe a pure state if and only if

$${\nu_x}^2 + {\nu_y}^2 + {\nu_z}^2 = 1. \tag{2.42}$$

Otherwise, it will describe a mixed state. Geometrically it follows that a pure state will be described by a vector moving on the Bloch sphere surface, while a mixed state will be described by a vector representing a point inside the sphere.

To examine the evolution of the Bloch vector in time we introduce (2.40) into the Liouvile equation to get

$$i\hbar\frac{d\hat{\nu}^B}{dt} = \frac{1}{2}Tr[\hat{\sigma}[H,(1+\hat{\nu}^B\cdot\sigma)]]. \tag{2.43}$$

When a static magnetic field B_z is applied, the solution of that equation shows that the Bloch vector will precess around the z-axis at the Larmor frequency, $\omega_L = \gamma B_z$, where γ is the gyromagnetic ratio of the atom. For simplicity, the dynamics of $\hat{\nu}^B$ may be calculated in a reference frame that rotates around the z-axis at the Larmor frequency.

The Bloch vector can also represent dissipation and dephasing of the two-state system. For that purpose, we define three additional parameters: the longitudinal relaxation time T_1, the transverse relaxation time T_2, and ${\nu_z}^0$, which is the z-component of the Bloch vector at thermal equilibrium. Adding these parameters to the equation of motion for $\hat{\nu}^B$ (2.43), and solving it in the rotating frame with no field except B_z, we obtain the following results for the components of the Bloch vector:

$$\nu_x(t) = \nu_x(0)e^{-\frac{t}{T_2}} \tag{2.44}$$

$$\nu_y(t) = \nu_y(0)e^{-\frac{t}{T_2}} \tag{2.45}$$

$$\nu_z(t) = \left(\nu_z(0) - {\nu_z}^0\right)e^{-\frac{t}{T_1}} + {\nu_z}^0. \tag{2.46}$$

This result is valid only in very simple cases, but it does convey the general picture. We see that if we start at t=0 in some pure state on the surface of the Bloch sphere, the projection of the Bloch vector on the xy-plane will start to shrink to zero according to the T_2 time constant, representing a dephasing or decoherence process. In parallel, but at a different rate defined by T_1, the z-component of the Bloch vector will decay towards its thermal equilibrium value ${\nu_z}^0$. Previously we described the probability oscillations created by an interaction applied to a two-level atom. Now we see that in order to observe such oscillations we have to fulfill the following requirements:

- We need an ensemble. Such an ensemble can be realized either by several measurements on a single atom or by one measurement of a group of atoms.

- We have to prepare our ensemble in a pure state. Otherwise, the atoms in the ensemble will have random phases relative to each other, and the observation of oscillations will be impossible. Such a preparation is usually made by some kind of optical pumping.
- We have to finish our measurements before decoherence and dissipation processes dominate, which means at a time shorter than the smaller of the two relaxation times T_1 and T_2.

2.1.6 Rabi pulses and Ramsey fringes

Focusing on the resonant case ($\delta = 0$), we can describe the effect on the Bloch vector due to an interaction applied for a time t using a 3×3 matrix [Kuh03]:

$$\hat{\nu}^B(t) = \Theta_{\theta(t)} \cdot \hat{\nu}^B(0) = \begin{pmatrix} 1 & 0 & 0 \\ 0 & \cos\theta(t) & \sin\theta(t) \\ 0 & \sin\theta(t) & \cos\theta(t) \end{pmatrix} \cdot \hat{\nu}^B(0) \tag{2.47}$$

where $\theta(t) = \int_0^{t'} \Omega(t')dt'$. In other words, the "Rabi pulse" rotates the vector around the x-axis. For $\theta = \pi$ and $\theta = \pi/2$ we get:

$$\Theta_\pi = \begin{pmatrix} 1 & 0 & 0 \\ 0 & -1 & 0 \\ 0 & 0 & -1 \end{pmatrix}, \Theta_{\pi/2} = \begin{pmatrix} 1 & 0 & 0 \\ 0 & 0 & 1 \\ 0 & -1 & 0 \end{pmatrix}. \tag{2.48}$$

If the Bloch vector initially lies on the sphere's surface and points up at the z-axis direction, corresponding to a full concentration of the population in the ground state, a π pulse will transform it to a vector pointing down at the z-axis direction, corresponding to a full inversion to the excited state (Fig. 2.3b). A $\pi/2$ pulse will take the vector halfway, to point in the y-direction (Fig. 2.3c). The system will then be in an equal superposition of the energy states. A second $\pi/2$ pulse, applied at this point immediately, will complete the population inversion to the excited state (Fig. 2.3d).

The matrix representation for the free precession (in the absence of the laser field) is

$$\Theta_{Free}(t) = \begin{pmatrix} \cos\phi(t) & \sin\phi(t) & 0 \\ -\sin\phi(t) & \cos\phi(t) & 0 \\ 0 & 0 & 1 \end{pmatrix}, \tag{2.49}$$

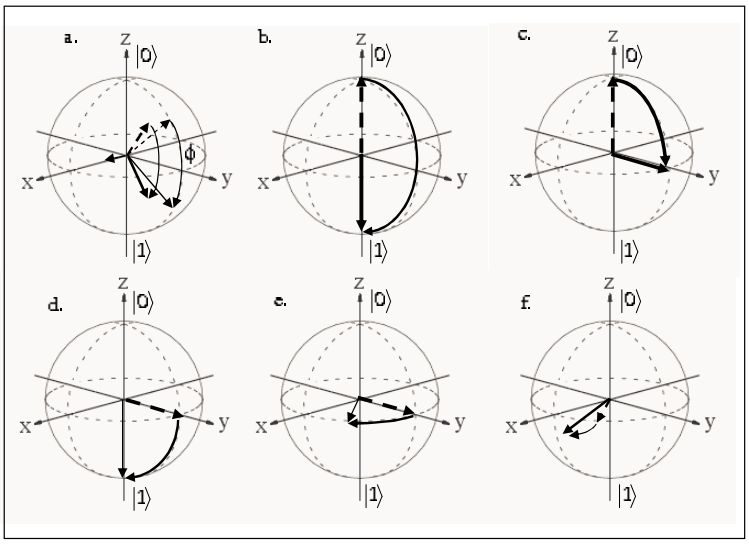

Figure 2.3: Examples of different Rabi pulses. The dashed line is the Bloch vector before the pulse, while the solid line is the Bloch vector after the pulse.

where $\phi(t) = \int_0^{t'} \delta(t')dt'$. The free-precession angular frequency of the Bloch vector will be $\delta = \omega - \omega_0$, as the dynamics during the interaction time were calculated in a rotating wave frame rotates at the laser frequency ω. The vector's precession represents the accumulated phase between the two states (Fig. 2.3e). In Fig. 2.3f the effect of that phase is shown: Initially indicating the ground state, the vector will not attain the excited state after two $\pi/2$ pulses, as it was allowed to precess in between.

Consider now the following sequence preformed on an ensemble of two-level atoms:

- The ensemble is prepared at the pure state $\psi(0) = |0\rangle$.
- A $\pi/2$ pulse is applied by a laser tuned to the frequency $\omega \approx \omega_0$.
- The laser is blocked for a period of time T.
- A second $\pi/2$ pulse is applied.
- The population P_1 in the excited state $|1\rangle$ is measured.

The Bloch vector, after this sequence, can be expressed using the matrices defined above:

$$\nu_{Ramsey}(T) = \Theta_{\pi/2} \cdot \Theta_{Free} \cdot \Theta_{\pi/2} \cdot \hat{\nu}^B(0). \tag{2.50}$$

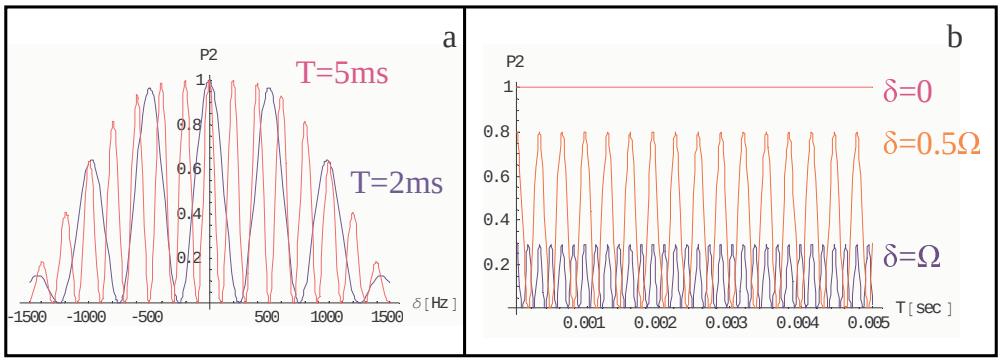

Figure 2.4: Ramsey fringes obtained by the variation of the detuning (a) and interrogation time (b) .

The population in state $|1\rangle$, indicated by the vector's z-component, will be affected by the accumulated phase during the interrogation time, namely,

$$\nu_{z,Ramsey}(T) = -\cos\phi = -\cos\left(\int_0^T \delta(t')dt'\right). \tag{2.51}$$

To observe oscillatory behavior of the population, we have to keep δ small enough compared to the Rabi frequency and the pulse width, such that the pulse can be approximated as near resonance, and complete population transfer can occur.

To understand the interferometric nature of the Ramsey method, one can compare it to a Mach-Zehnder interferometer consisting of two 50/50 beam splitters (BS) and a laser beam. The affect of the first $\pi/2$ pulse is similar to the first BS, as it splits the atomic wave function into a superposition of the two states. The interrogation time is analogous to the free propagation of the beam in the MZ interferometer. During this time, the relative phase between the two states evolves at a rate relative to the energy difference between them, and the coupling field accumulates a phase of ωT. The second $\pi/2$ pulse combines the two states again, to get the "interference" pattern known as Ramsey fringes.

In Fig. 2.4a we show the (calculated) Ramsey fringes where the detuning is varied from -1500 Hz to +1500 Hz, with Rabi frequency of $\Omega = 2\pi\cdot 1000$ Hz. The two curves of the population in the excited state ($P_2 = (1 - \nu_{z,Ramsey})/2$) against the detuning are plotted for two different interrogation times. The width of the fringes is given by $\Delta_\nu = 1/2T$. In Fig. 2.4b we show the fringes as a function of the interrogation time T. Note that in the resonant case a full population inversion occurs with no dependence on the interrogation time.

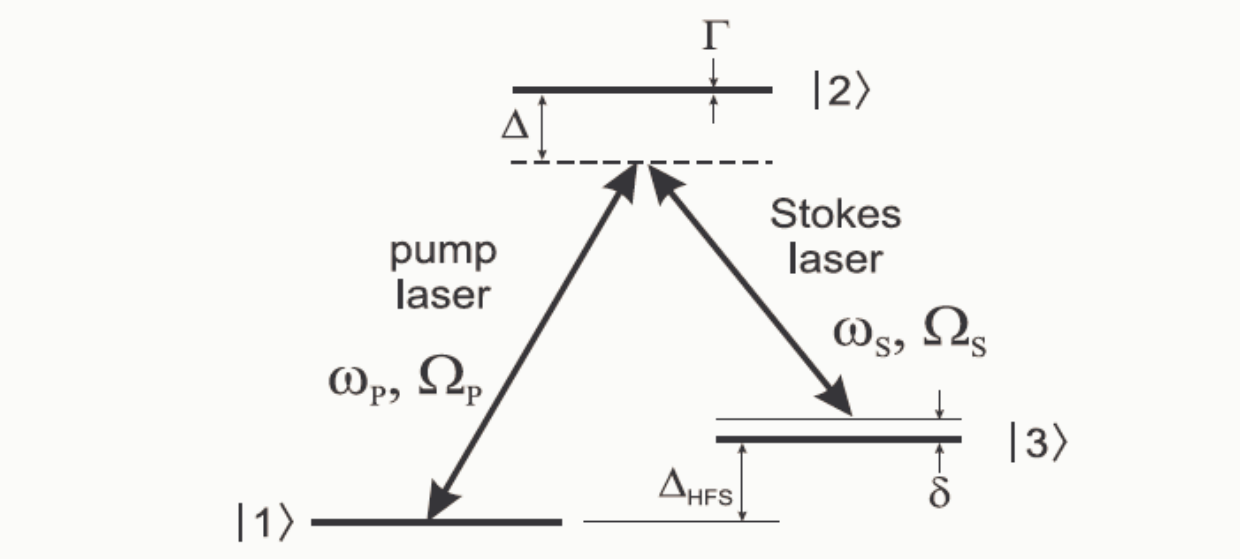

Figure 2.5: 3-level system in a Λ-configuration.

2.2 Stimulated Raman transitions

A Raman transition couples two atomic levels by the absorption of a photon from one laser beam (pump beam) and by stimulated emission of another photon into the other beam (Stokes beam). Fig. 2.5 shows a three-level atom in a laser field consisting of two beams in a Λ-configuration. The pump beam couples levels $|1\rangle$ and $|2\rangle$, while the Stokes beam couples levels $|3\rangle$ and $|2\rangle$. As a result the levels $|1\rangle$ and $|3\rangle$ become coherently coupled by the Raman beams.

To avoid resonance excitation the detuning Δ of the Raman beams from the one-photon transition has to be much larger than the line width Γ. Both Raman beams are characterized by the Rabi frequency Ω_i. If the optical frequencies of the Raman beams are ω_P and ω_S, respectively, the Raman detuning δ is defined as the detuning from the two-photon resonance.

2.2.1 The basics of Raman transitions

To describe the coherent evolution of the Λ-system we construct the Hamiltonian and solve the corresponding TD Schrödinger equation (2.9).

The hamiltonian describing that system (using the rotating wave approximation) [Sho90], is given by

$$\hat{H} = \frac{\hbar}{2}\begin{pmatrix} 0 & \Omega_P & 0 \\ \Omega_P & 2\Delta & \Omega_S \\ 0 & \Omega_S & 2\delta \end{pmatrix}, \tag{2.52}$$

where Ω_P and Ω_S are the Rabi frequencies induced by the pump and the Stokes beams respectively. The state vector of the three-level atom, $\Psi(t)$, can be expressed as a superposition of the three orthogonal eigenstates of H_0 (the unperturbed Hamiltonian), namely

$$\Psi(t) = C_1(t)\psi_1 + C_2(t)\psi_2 + C_3(t)\psi_3. \tag{2.53}$$

Introducing (2.52) and (2.53) into the TD Schrödinger equation we get three coupled equations for the probability amplitudes $C_i(t)$:

$$\begin{cases} i\dot{C}_1(t) = \frac{1}{2}\Omega_P C_2(t) \\ i\dot{C}_2(t) = \frac{1}{2}(\Omega_P C_1(t) + \Omega_S C_3(t)) + \Delta C_2(t) \\ i\dot{C}_3(t) = \frac{1}{2}\Omega_S C_2(t) + \delta C_3(t) \end{cases} \tag{2.54}$$

Since Δ is much larger than the Rabi single-photon frequencies, the population in the excited level $|2\rangle$ will undergo much faster oscillations than the other populations. Thus, we can replace $\dot{C}_2$ with its average over a large number of cycles, namely zero. This approximation, known as "adiabatic elimination", reduces our system to an effective two-level system

$$\begin{cases} i\dot{C}_1(t) = \frac{\Omega_P}{4\Delta}(\Omega_P C_1(t) + \Omega_S C_3(t)) \\ i\dot{C}_3(t) = -\delta C_3(t) + \frac{\Omega_S}{4\Delta}(\Omega_P C_1(t) + \Omega_S C_3(t)) \end{cases} \tag{2.55}$$

described by the effective Hamiltonian

$$\hat{H}_{EFF} = \frac{1}{4}\begin{pmatrix} {\Omega_P}^2/\Delta & \Omega_P\Omega_S/\Delta \\ \Omega_P\Omega_S/\Delta & {\Omega_S}^2/\Delta - 4\delta \end{pmatrix} \tag{2.56}$$

The off-diagonal elements of the Hamiltonian indicate the coupling between the levels $|1\rangle$ and $|3\rangle$ due to the laser interaction, while the diagonal elements indicate the shift of each energy state, due to the interaction with the far red detuned laser. The shift of the two-photon transition is thus given by

$$\delta_{diff} = \frac{{\Omega_P}^2}{4\Delta} - \frac{{\Omega_S}^2}{4\Delta}. \tag{2.57}$$

Solving (2.55) while assuming that all the atoms are initially in level $|1\rangle$, we get the time-dependent populations

$$\begin{cases} P_1(t) = |C_1(t)|^2 = 1 + \frac{1}{2}\frac{{\Omega_R}^2}{{\Omega_0}^2}[\cos\Omega_0 t - 1] \\ P_3(t) = |C_3(t)|^2 = \frac{1}{2}\frac{{\Omega_R}^2}{{\Omega_0}^2}[1 - \cos\Omega_0 t] \end{cases} \tag{2.58}$$

where $\Omega_R = \Omega_P\Omega_S/2\Delta$ is the two-photon resonant Rabi frequency and $\Omega_0 = \sqrt{{\Omega_R}^2 + \delta^2}$ is the generalized Rabi frequency. These equations describe an oscillating probability to find the atom in one of the levels. A complete inversion of the population from level $|1\rangle$ to level $|3\rangle$ will occur when the Raman detuning is zero.
The width of the transition is given by the range of the Raman detuning where the oscillation amplitude is larger than 1/2, namely

$$\Delta\omega_{power} = 2\Omega_R. \tag{2.59}$$

As Ω_R depends on the laser intensities, this broadening can be referred to as power broadening.

2.2.2 Scattering rate

In spite of the large detuning of the Raman beams from the atomic single-photon resonance, they can still excite the atomic transitions. The affect of the Raman beams can be evaluated by the scattering rate [Ste01]. A laser beam coupling characterized by Rabi frequency Ω and detuning Δ from the one-photon transition produces a scattering rate of

$$\Gamma_{sc} = \frac{\Gamma}{2}\frac{(\Omega/\Gamma)^2}{1 + 4(\Delta/\Gamma)^2 + (\Omega/\Gamma)^2}, \tag{2.60}$$

where Γ is the line width of the excited level. For large detunings, (2.60) reduces to

$$\Gamma_{sc} = \frac{\Gamma}{2}\frac{\Omega^2}{4\Delta^2}. \tag{2.61}$$

This means that the scattering rate (proportional to Δ^{-2}) will be supressed much faster than the two-photon Rabi frequency (proportional to Δ^{-1}), as the detuning is increased.

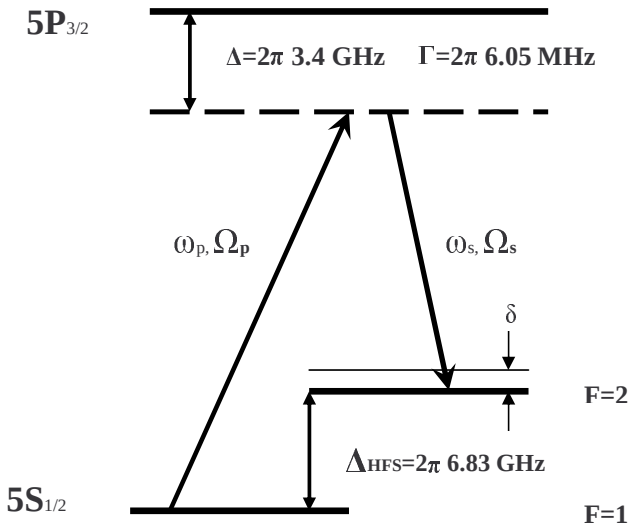

Figure 2.6: 2-photon Raman transition connecting the two hyperfine levels of ^{87}Rb ground state

2.2.3 Raman transitions in rubidium atoms

In our experiments we manipulate rubidium atoms employing the D2-transition, at 780 nm, between the $5S_{1/2}$ and $5P_{3/2}$ states. We are particularly interested in this transition rather than the D1-transition because we intend to apply our system to cold atoms and the cooling is achieved by many cycles of absorption and subsequent emission of photons between the $F = 2$ and $F' = 3$. Atoms that are lost from the cooling cycle are repumped to the $F = 2$ level by a second laser tuned to the $F = 1 \rightarrow F' = 2$ transition. The first excited state, $5P_{1/2}$, is only split into two hyperfine levels, therefore this cooling process is not possible through the D1 transition.

To coherently manipulate the rubidium ground-state hyperfine levels we use the Raman transition as shown in Fig. 2.6. The typical detuning of the Raman beams from the D2 transition is much larger than the linewidth of the excited state: $\Delta = 2\pi{\cdot}3.4$ GHz $\gg$ $\Gamma = 2\pi{\cdot}6.065$ MHz. In the absence of an external magnetic field, the hyperfine states are degenerate with respect to spin orientations. The dependence of the Rabi frequency on the initial m_F sublevels and the polarizations of the Raman beams is defined by

$$\Omega_{R,0} = \Omega_R \sqrt{X(m_F)} = \frac{\Omega_P \Omega_S}{2\Delta} \sqrt{X(m_F)} \tag{2.62}$$

where the coefficient $X(m_F)$ is given by [Mue01]

$$\begin{cases} \frac{1}{288}(2+m_F)(3+m_F) & : (\pi,\sigma^-),(\sigma^+,\pi) \\ \frac{1}{288}(2-m_F)(3-m_F) & : (\pi,\sigma^+),(\sigma^-,\pi) \\ \frac{1}{36}[1-(\frac{m_F}{2})^2] & : (\sigma^+,\sigma^+),(\sigma^-,\sigma^-) \\ 0 & : (\pi,\pi),(\sigma^\pm,\sigma^\mp) \end{cases} \tag{2.63}$$

where symbols in parentheses (to the right of the colons) denote the polarizations of the two Raman lasers.

2.2.4 The $\Delta m_F = 2$ problem

Using the Zeeman sub-levels of the rubidium ground state, $|F=1, m_F=-1\rangle$ and $|F=2, m_F=1\rangle$, as the qubit states, $|0\rangle$ and $|1\rangle$, respectively, is of special interest to us for the following reasons:

- Atoms in both states can be trapped by magnetic potential (i.e. they are low-field seekers).
- The magnetic moments and the corresponding static Zeeman shifts of the two states are approximately equal, leading to a strong common mode suppression of magnetic field induced decoherence.

Note: Beyond the first-order approximation, the slopes of the magnetic shift curves $\Delta_\nu(B)$ of states $|0\rangle$ and $|1\rangle$ are field dependent. At $B_0 \approx 3.23$ G the slopes of those curves are equal. Thus, when the magnetic field at the trap bottom is B_0, the frequency shift between the trapped states remains nearly constant along the atomic cloud, and the effect of field fluctuations is greatly reduced.

To realize the $|\Delta m_F = 2|$ transition one needs to drive a two-photon interaction. It can be done using a combination of microwave and RF fields, in a scheme described in Fig. 2.7 [Tre06]. The microwave field couples the qubit state $|0\rangle$ and the intermediate state $|F=2, m_F=0\rangle$, while the RF photon couples the intermediate state and the qubit state $|1\rangle$. As a result, the states $|0\rangle$ and $|1\rangle$ are coherently coupled. In order to prevent scattering from the intermediate state, both fields are 1.2 MHz detuned from the one-photon transition.

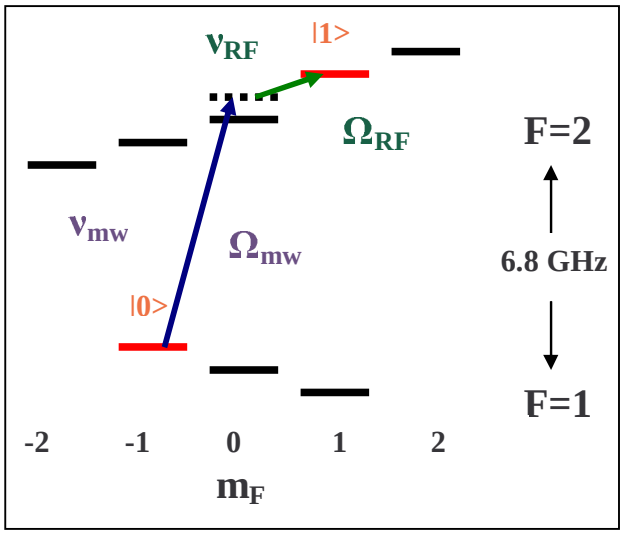

Figure 2.7: Scheme of a Raman transition coupling the states $|0\rangle$ and $|1\rangle$, using microwave and RF fields.

However, this method has very poor spatial resolution, because of the large wavelength of the RF and microwave radiation.

Much higher spatial resolution can be achieved using a Raman scheme based on optical-range laser beams (see Fig. 2.6). The higher resolution is due to the possibility of focussing the laser beam to a waist of a few micrometers. However, use of optical laser beams has its own problem: A $|\Delta m_F = 2|$ transition requires spin flips of both the electron and the nucleus, while the laser light interacts only with the electron. The flipping of the nuclear spin can be achieved only through the hyperfine interaction between the electron and the nucleus. To complete the flipping, the atom has to occupy the excited state (in our case the $5P_{3/2}$ state) for a period of time proportional to the inverse of the hyperfine splitting energy of the excited state.

On the other hand, we would like to avoid the occupation of the excited state during the Raman transition, as it leads to spontaneous emission. For this reason the Raman beams have to be significantly detuned ($\sim$10 GHz) from the excited state. This will reduce the probability of a nuclear spin flip, driving the transition amplitude to zero.

A scheme of the two laser beams for a $|\Delta m_F = 2|$ Raman transition is presented in Fig. 2.8. Selection rules allow a two-photon transition from $|\mathbf{A}\rangle = |F = 1, m_F = -1\rangle$ to $|\mathbf{B}\rangle = |F = 2, m_F = 1\rangle$ only via $|\mathbf{C}\rangle = |F' = 1, m_F = 0\rangle$ and $|\mathbf{D}\rangle = |F' = 2, m_F = 0\rangle$. A σ^+ laser beam

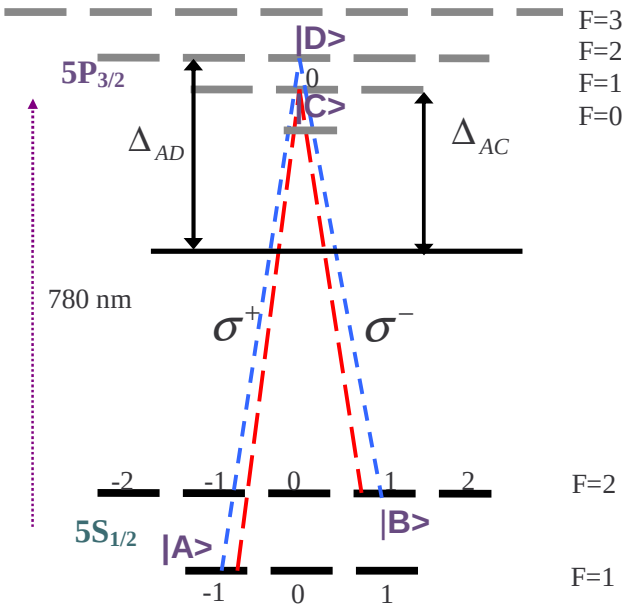

Figure 2.8: A scheme of the $|\Delta m_F = 2|$ Raman transition

with the frequency ω_1 is tuned between $|\mathbf{A}\rangle$ and the excited state, with detunings Δ_{1C} and Δ_{1D} from levels $|\mathbf{C}\rangle$ and $|\mathbf{D}\rangle$ respectively, while a σ^- laser beam with the frequency ω_2 is tuned between $|\mathbf{B}\rangle$ and the excited state, with the detunings Δ_{2C} and Δ_{2D}. The effective Rabi frequency of the process is thus a sum over the two Raman transitions, namely

$$\Omega_{AB} = \frac{\Omega_{AC}\Omega_{BC}}{2\Delta_C} + \frac{\Omega_{AD}\Omega_{BD}}{2\Delta_D}, \tag{2.64}$$

where we set $\Delta_{2C} \approx \Delta_{1C} \equiv \Delta_C$ and $\Delta_{2D} \approx \Delta_{1D} \equiv \Delta_D$ for the near-resonant case. The electric diploe matrix elements relevant to that transition satisfy [Ste01]

$$\langle B|\mathbf{d}\cdot\mathbf{E}|C\rangle\langle C|\mathbf{d}\cdot\mathbf{E}|A\rangle + \langle B|\mathbf{d}\cdot\mathbf{E}|D\rangle\langle D|\mathbf{d}\cdot\mathbf{E}|A\rangle = 0, \tag{2.65}$$

followed by $\Omega^*{}_{BC}\Omega_{AC} + \Omega^*{}_{BD}\Omega_{AD} = 0$. Introducing this relation, Eq. (2.64) reduces to

$$\Omega_{AB} = \frac{1}{2}\Omega_{AC}\Omega_{BC}\left(\frac{1}{\Delta_C} - \frac{1}{\Delta_D}\right), \tag{2.66}$$

and since $\Delta_D = \Delta_C + (E_D - E_C)/\hbar$, we can write

$$\Omega_{AB} = \frac{1}{2}\Omega_{AC}\Omega_{BC}\frac{(E_D - E_C)/\hbar}{\Delta^2}, \tag{2.67}$$

where Δ is the average value of Δ_C and Δ_D. We can thus see that for a detuning much larger than the hyperfine splitting of the excited state, the effective Rabi frequency will go to zero.

Pulse no.	Pulse area (θ)	Relative phase (φ)
1	π/√2	0
2	π	π/2
3	π/√2	0
4	π	π/2

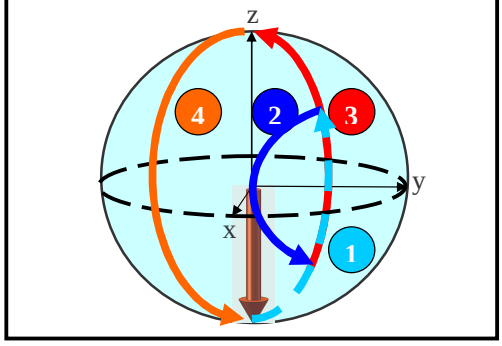

Figure 2.9: The pulse sequence demonstrated in the Bloch picture.

2.2.5 An example: Coherent control of the atomic state

Two phase-locked Raman beams can be used to manipulate a two-state system. In Fig. 2.9 we demonstrate the rotation of the atomic state as a result of a sequence of Raman pulses. The pulse lengths θ (see definition in Sect. 2.1.6) and relative phases ϕ are specified in the attached table. The Raman pulse corresponds, in the Bloch representation, to a rotation around an axis in the XY-plane (see appendix A). This axis is determined by the relative phase between the Raman beams. Relative phases of zero and $\pi/2$ correspond to rotations around the X and Y axes respectively. Controlling the phase of each pulse in the sequence enables us to change the axis of rotation of the Bloch vector. This is well demonstrated in the sequence described in Fig. 2.9.

Chapter 3

The experimental system

3.1 General structure of the system

The basic structure of our experimental system is described in Fig. 3.1. With this system we study the affects of the radiation field on the atomic medium. The radiation field is induced either by the microwave signal generator or by the Raman laser subsystem. We use the probe laser both to prepare the atomic medium before it interacts with the radiation field and to measure the effects of this interaction. The final output is a graph of the atomic population versus the time of interaction of the atomic medium with the radiation field.
The microwave and the Raman laser subsystems will be discussed in Chaps. 4-5 respectively. In this chapter we review the system elements: lasers used in the experiment, experimental sequence and the population detection technique.

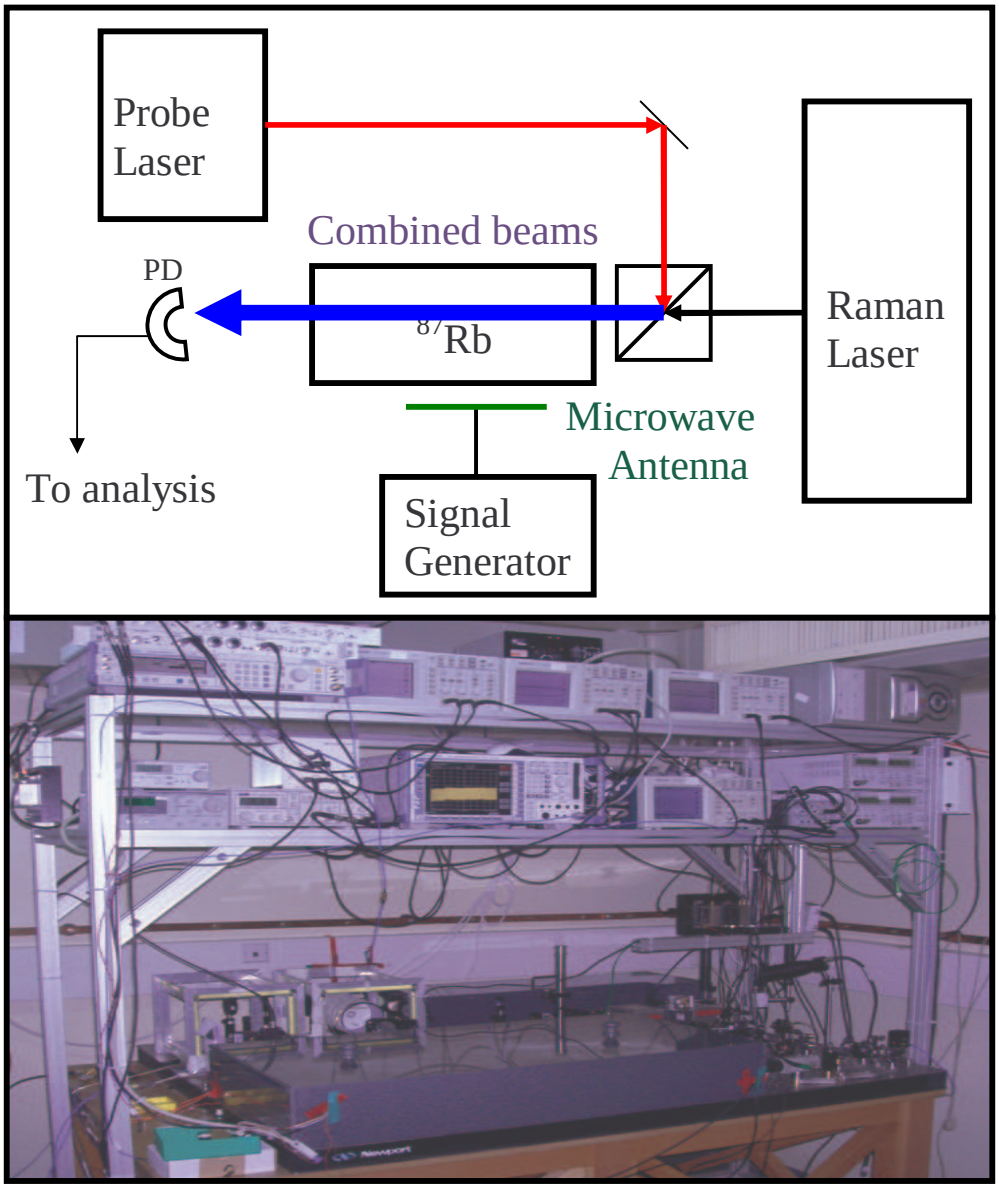

Figure 3.1: A scheme and a photo of the experimental system

3.2 Lasers and laser locking

Laser diodes have become commonly used in atomic physics, since they supply the demand for wavelength stability and narrow linewidth. To lock a laser on an atomic transition, one would like the laser linewidth to be much narrower than the transition's natural linewidth. In the case of alkali atoms, that means less than 1 MHz laser linewidth (The linewidth of the D2 line transition of ^{87}Rb, for example, is Γ=6.065 MHz), which can be easily achieved by a low cost, home made external cavity diode laser. By using a feedback loop, these lasers can be frequency locked to an atomic transition.
In the following section we will first review the basic properties of a laser diode and an external cavity diode laser (ECDL) then present the properties of the lasers we built for our experiment. Finally, we will introduce the theory of polarization locking, which is the locking method we use, and show results from our locking system.

3.2.1 Laser diodes

Most of the laser diodes used in spectroscopy today, are designed in the quantum well configuration. A quantum well is obtained by a p-type and an n-type semiconducting material, separated by a thin layer of another semiconductor material. This middle layer is called the active layer. If the quantum well is forwardly biased by electric current injection, population inversion is achieved. This means that the density of charge carriers in the conduction band is higher than the density of charge carriers in the valence band. The carrier pairs that recombine in the active layer can emit a photon. If this emission is induced by the presence of other photons it is called stimulated emission. When the rate of that stimulated emission is higher than the absorption rate, an optical gain is achieved. If the optical gain is sufficiently large, that is if the injected current is large enough, the semiconductor will act as a laser.
Since the refractive index of the semiconductor is different from that of the surrounding air, some of the light will be reflected back from the diode surface (the diode can be AR coated to prevent those reflections). The diode therefore operates like an optical resonator, which means that it lases in certain modes. The different modes arise from the fact that several wavelengths can exactly fit in the cavity. The phase shift imparted by a single round trip

must therefore be a multiple of 2π. This phase shift φ due to one round trip in the cavity is given by

$$\varphi = \frac{2\pi\nu}{c} 2nL \tag{3.1}$$

where L is the cavity length, and n is the refractive index. Introducing the condition $\varphi = 2\pi m$ (m is an integer), we get the frequency of the m-mode:

$$\nu_m = \frac{mc}{2nL} \tag{3.2}$$

The emission wavelength of the laser will be determined by the competition between the different modes. The distance between 2 neighbor modes is called the free spectral range, and can be found by replacing m by 1 in Eq. (3.2).

An AlGaAs/GaAs laser diode (which is the kind we used in our experiment) has a typical cavity length L of 300 μm and a refractive index n of about 3.5. Due to this high refractive index the reflection coefficient is about 30%. At the wavelength of 780 nm, the frequency is 384 THz and the mode number is around 3×10^3. The free spectral range is approximately 150 GHz and the modes bandwidth is about a few tens of MHz [Ric95].

The lasing wavelength can be controlled by both the diode temperature and the injection current. The variation of the diode temperature has two different effects on the energy bandgap. First, it changes the lattice constant due to thermal expansion. Second, it effects the vibrations of the diodes which in turn effects the bandgap. A change in the temperature also effects the cavity length [Ric95]. A change in the current injected to the diode, induces a variation of the carrier density which leads to a change in the refractive index and as a result, a change in the emission wave length. The diodes we used in our experiment have a typical 1.5 GHz/mA and $0.25nm/^\circ C$ tuning rates of current and temperature, respectively. We cannot however, control the laser wavelength well enough only by tuning its temperature and current, since it operates in several modes. While tuning the frequency, a mode hope can occur, which means the laser starts to operate in another mode. That may make some frequency domains inaccessible. Another undesirable effect is the hysteresis of the laser diode. This means that wavelength variation as a function of the temperature depends on whether the temperature is increased or decreased.

3.2.2 External Cavity Diode Lasers (ECDL)

Diode lasers are very susceptible to optical feedback, a technique that can be used to create a tunable, narrow linewidth laser source. Such a feedback can be achieved using a diffraction grating in the Littrow configuration (see Fig. 3.2). The grating is positioned in front of the diode laser in a certain angle, such that the first diffraction order is reflected back to the diode, while the zero-th order is outcoupled. In our experiment we use a holographic grating that produces a back reflection of 21%, while 62% are outcoupled. The loss due to absorption is therefore 17%. Taking that external cavity's length L to be 3 cm, we can decrease our FSR from 150 GHz (for solitary laser diode) down to 5 GHz. Furthermore, the bandwidth is reduced to less than 1 MHz by using the grating.
Besides of the variation of the injection current and the diode temperature, we can tune the ECDL wavelength by aligning the angle between the grating and the beam (the angle α in Fig. 3.2). The frequency of the beam reflected by the grating will follow [Jen76]

$$\nu_g = \frac{pc}{2d \sin \alpha} \tag{3.3}$$

where p is the diffracted order and d is the grating constant. This dispersive property of the grating makes it select one of the laser diode's modes for optical feedback, As this mode experiences the lowest loss. In our lasers we used gratings with 1800 lines per mm ($d = 0.55\mu m$), which means that in order to get a wavelength of 780 nm, the angle of incidence should be aligned to 45.25°.
The resolving power of the grating is given by

$$\frac{\nu_g}{\Delta\nu_g} = pN \tag{3.4}$$

where N is the number of lines illuminated by the laser beam. With beam diameter of 4 mm, we get that $N = 7270$. This means that the grating provides feedback over a bandwidth of $\Delta\nu_g$ =53 GHz. Since the mode separation of the solitary diode modes is 150 GHz, only one of this modes lies beneath the grating profile. Obviously the grating profile has to be within the bandwidth of the diode gain profile which is typically 10nm.

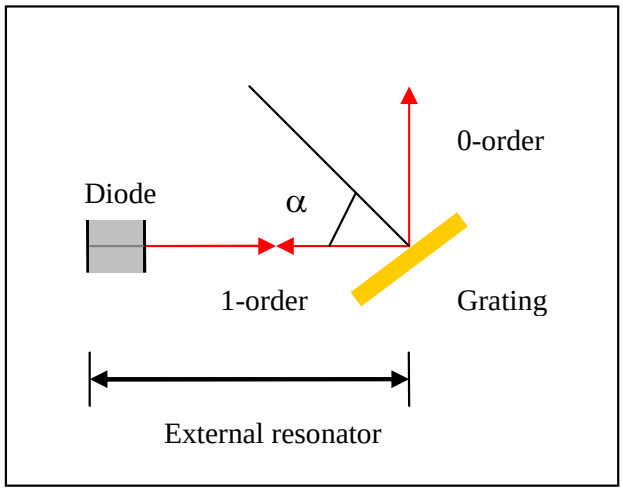

Figure 3.2: A scheme of an ECDL in the Littrow configuration

3.2.3 Lasers in the experiment

Our system includes four lasers. Two of those lasers are ECDL's designed in the Littrow configuration, and two are slave lasers. One of ECDL's is used as a master laser, to inject two slave lasers. The two slave beams serve as the pump and the Stokes beams that induce the Raman transition (see Sect. 2.2). The second ECDL serves as a probe laser to detect population variations in the atomic levels. The types of laser diodes used in the experiment are $SHARP\ GH0-781-JA2C$ and $SANYO\ DL7140-201S$. Although the Sharp diode is more powerful (maximum power of 150 mw comparing with 100 mw of the Sanyo diode), we found the Sanyo diode to be more stable in the long term.

Master and probe Lasers

The mechanical arrangement of our grating stabilized laser diode system is shown in Fig. 3.3. The laser diode is mounted inside a collimation tube that has an adjustable lens in its front end. The tube is glued into a hole in an aluminium made diode mount. The temperature control system includes a Thermo Electric Cooling (TEC) element located between the diode mount and a metal base (serving as a heat sink), a PID temperature controller ($ThorLabsTED200$), and a thermistor located in the diode mount. The current injected to the diode is controlled by $ThorLabsLCD200$. The diffraction grating, located in front of the diode, can be coarsely adjusted by the adjustment screws. For fine tuning we use a PZT element connected to a home made high voltage amplifier. The entire set-up is covered

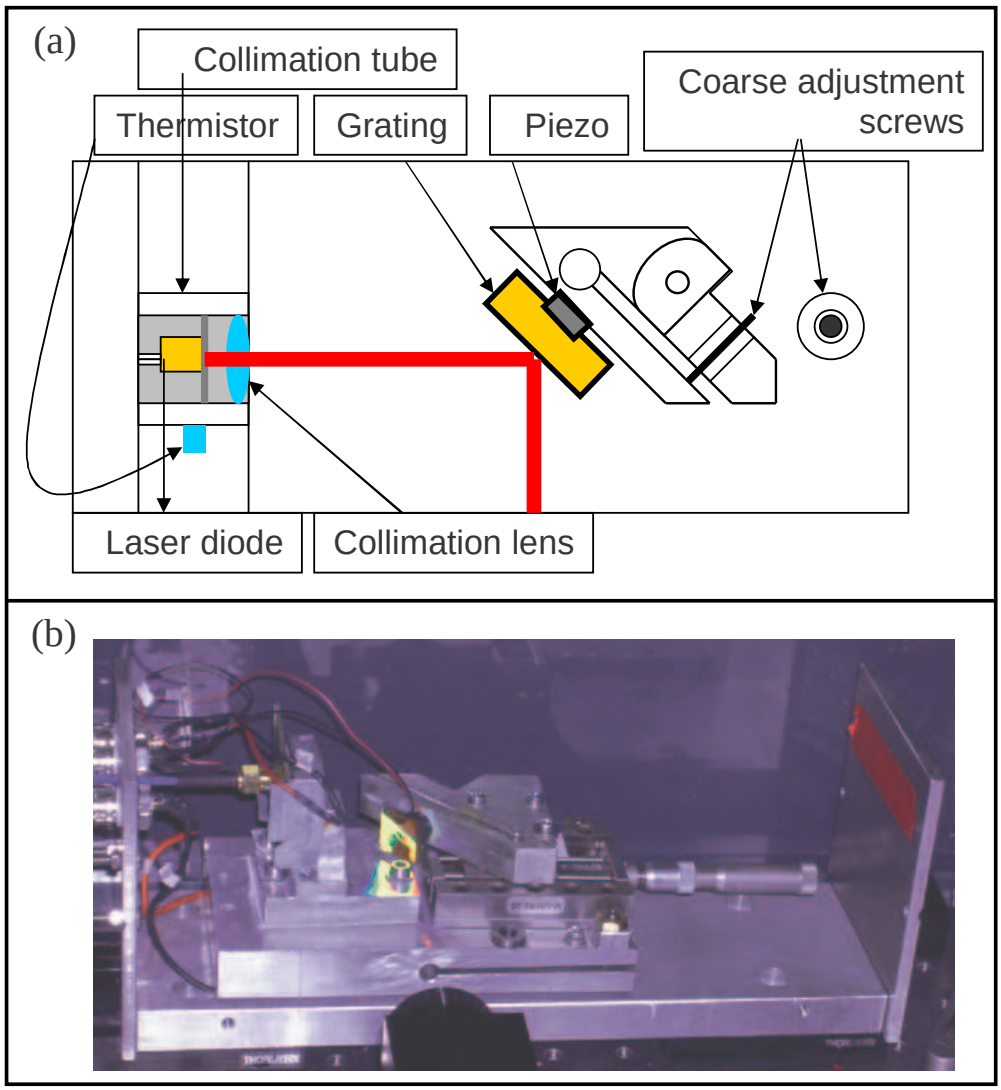

Figure 3.3: (a) A scheme of the ECDL used in the experiment. (b) A photo of our master laser (ECDL on a translation stage).

by an aluminium shield to protect it against dust, RF noise and temperature drifts of the surrounding air. In the master laser setup only, the grating was mounted on a translation stage to let us change the cavity length on a millimetric scale (see Fig. 3.3b).

The laser beam emitted by the diode has an elliptical shape. When we mount the diode we have to make sure the major axis of the elliptical beam is perpendicular to the grating lines. To collimate the beam we monitored its size and shape for few meters along the optical path, while adjusting the collimation lens. The beam is well collimated if it keeps its size and elliptical shape over a long distance.

To align the grating we projected the laser beam on a screen. If the grating is misaligned we will see two spots: The bright outcoupled zeroth order produces one spot, and second spot is the image of the first order beam reflected by the backside of the laser diode. To make sure the first order is back reflected to the diode we have to combine the spots by adjusting the grating position. The best overlap between the beams is indicated by a minimum threshold operation current of the laser.

The horizontal adjustment screw of the grating is used also for coarse wavelength tuning. While we scan for the desired wavelength, we may spoil a beat the overlap of the beam orders (which is done by the same screw), but since the size of the beam is relatively large (around 4 mm), a reasonable, even if not optimal, overlap is still maintained.

To find the optimal current and temperature settings for our laser operation, we did the following measurements. First, we kept the injection current fixed and scanned the laser temperature between $15°C$ and $20°C$. The results (for the master laser) are shown in Fig. 3.4a.

Our operating wavelength is 780.24nm (the wavelength of the D2 line, see Fig. 3.5). From the graph we see that we can choose several temperature points to work at. The optimal temperature will be as close as possible to our lab ambient temperature (around $20°C$), so as to increase stability and prevent condensation.

In Fig. 3.4b we see the variation of the wavelength as a function of the current, while the temperature is fixed. This graph demonstrates another advantage of the external cavity configuration. The tuning rate of the wavelength is now 0.2 GHz/mA, comparing to a typical rate of 1.5 GHz/mA for the independent diode. The resolution of wavelength is therefore

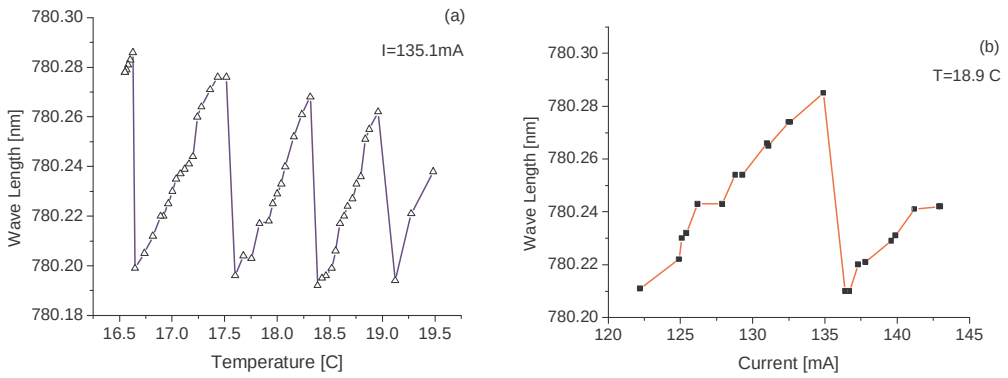

Figure 3.4: The variation of the master Laser wavelength, against temperature (a) and current(b).

improved. The Free Spectral Range (FSR) extracted from the graph is 4.2 GHz, which is in good agreement with the typical value for this kind of diodes (5 GHz).

In the course of the wavelength tuning, we sometimes noticed that the laser operates in multimode, i.e the laser emits light in several competing modes. In such a case we had to modify the current and/or temperature settings. If that didn't help we had to realign the external cavity, and sometimes even change the diode.

Fine scanning of the laser wavelength is done by applying a triangle waveform voltage on a piezoelectric element (PZT) located behind the grating (see Fig. 3.3a). The PZT expands under the applied voltage, changes the cavity length and by that also the wavelength of the emitting mode. The scanning range of the wave length has to be within the bandwidth of the grating or a mode hop will occur. In our experiments a maximum Free Mode Hop Range (FMHR) of $\sim$ 8 GHz was achieved but we had hard time reproducing it. Anyway, to lock a laser on a certain frequency such a FMHR is preferable but not necessary, since the linewidth of the locked laser is less than 1 MHz, and the width of the peak we lock the laser on is in the order of the natural linewidth ($\sim$ 6 MHz). A FMHR of 3 GHz, which is easy to reproduce, turned out to satisfy our experimental demands.

Slaves

The slaves are simply solitary diode lasers. Their emission wavelength is tuned only by current and temperature. The characterization of the wavelength for one of the slaves is shown in Fig. 3.6. The wavelength is linear with the injection current, but sometimes a mode hop may occur. The mode hop marked in the graph by a blue arrow corresponds to an FSR

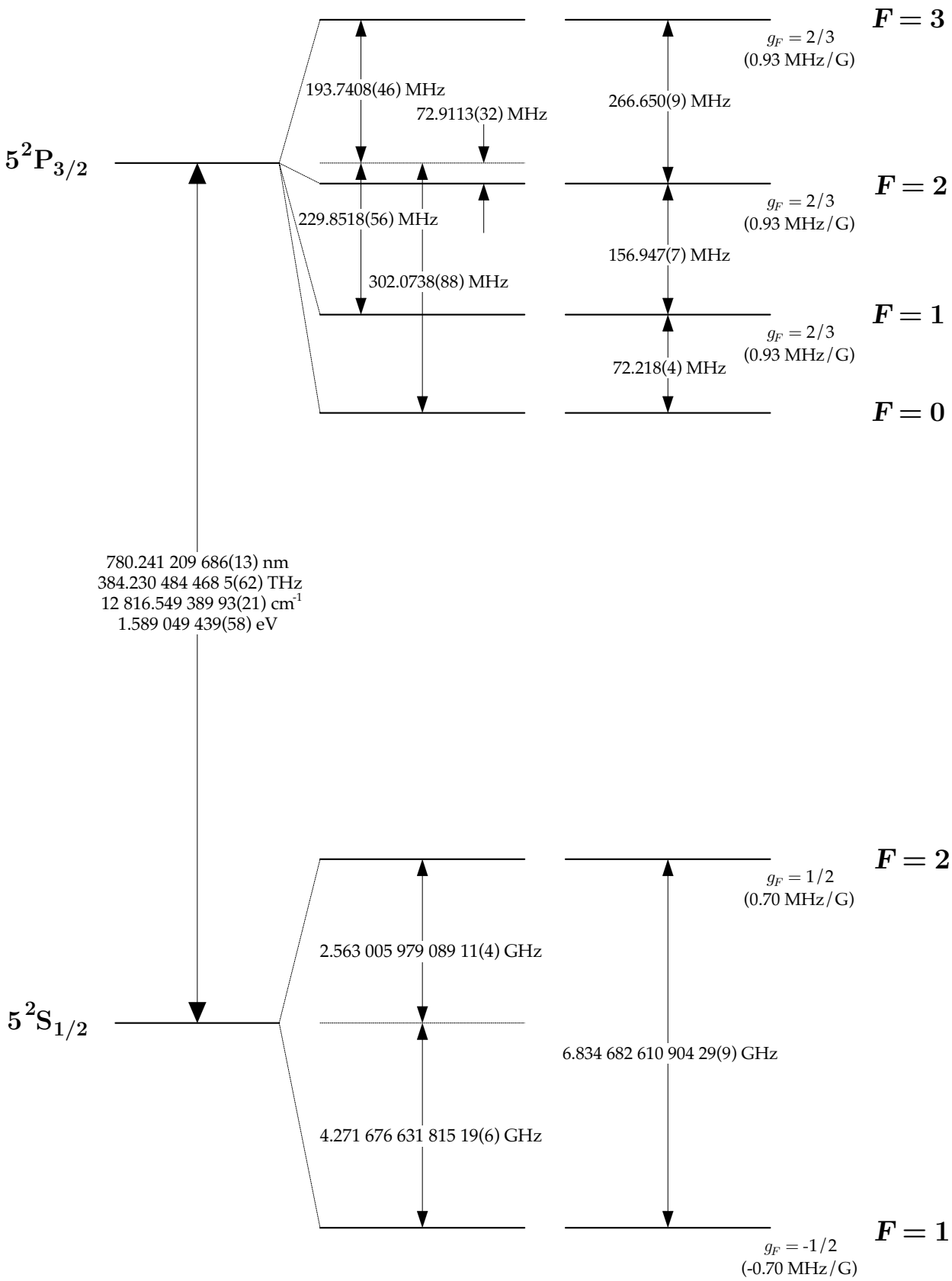

Figure 3.5: A diagram of the D2 line transition of ^{87}Rb

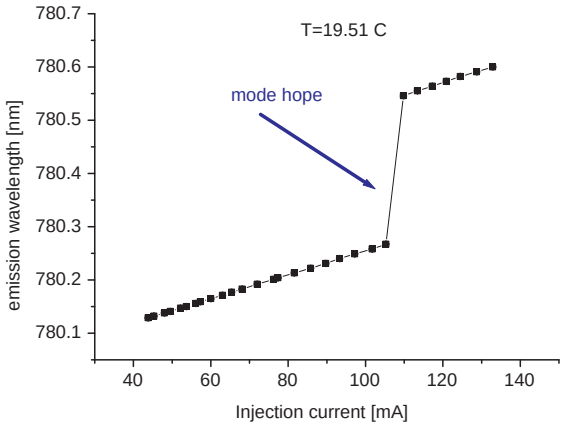

Figure 3.6: The emission wavelength of a slave laser as a function of the injection current. The temperature of the diode during the measurements was 19.51°C

of ∼140 GHz which is in good agreement with the typical value reported for this kind of diodes (150 GHz). The tuning rate calculated from the curve slope is 1.28 GHz/mA (the typical value is 1.5 GHz/mA). Note the differences in the wavelength tuning rates and FSR, comparing to the ECLD characteristics (Fig. 3.4).

3.2.4 Polarization lock

In order to keep the ECDL frequency fixed (typical drifts are from the order of several GHz/hr), We lock it on an atomic transition reference through a feedback loop. This can be done by several methods.

To lock our lasers we have used the polarization lock technique. In this technique we use polarization spectroscopy to create an error signal. That signal is fed back to the PZT through a PID loop and a high voltage amplifier and by that also stabilize the wavelength. Unlike Frequency Modulation (FM) methods, this technique does not require any modulation of the laser light. Thus, the polarization lock method does not add unwanted noise to the laser beam, while maintaining a linewidth of less than 1 MHz.

Polarization spectroscopy is a method of high resolution spectroscopy, similar in many ways to saturation absorption spectroscopy [Pet98]. The medium is pumped and probed with two beams created from the same laser, with the pump beam more intense than the probe.

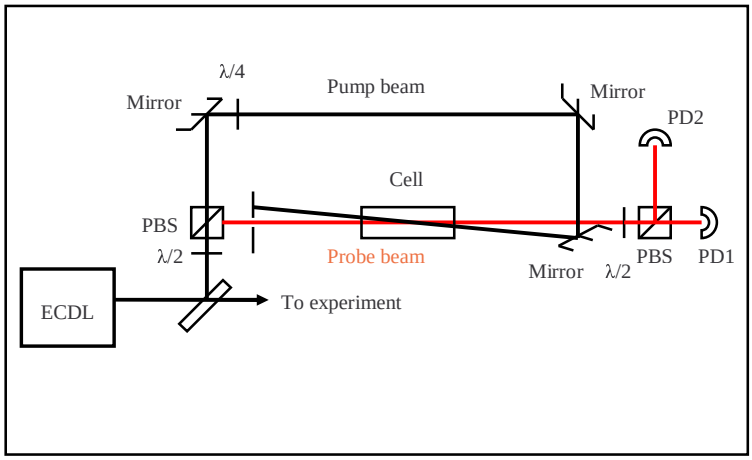

Figure 3.7: A scheme of the Polarization spectroscopy setup

The differences between the spectroscopic methods are in the pumping and probing mechanisms. The theory concerning polarization spectroscopy is examined in depth in [Dem03] and [Pea02].

In Fig. 3.7 our polarization spectroscopy setup is shown. The ratio between the probe and pump beams is controlled, by a half wave plate and a Polarizing Beam Splitter cube (PBS). A ratio of approximately 1:3 (the intensity of the pump is ∼3 mw) was found to provide the best signal in our setup.

The pump beam passing through the cell is circularly polarized by a $\lambda/4$ plate, while the probe beam is linearly polarized. It is important to note that the linear probe light can also be considered as a superposition of σ^+ and σ^- components.

The circularly polarized pump light will induce $\Delta m_F = -1$ and $\Delta m_F = +1$ transitions in the atomic sample, for σ^- and σ^+ beams respectively. The atoms will be therefore "pushed" to the highest or lowest m_F states. The result is that the medium now has a non-uniform population in the different magnetic sub-levels. A linearly polarised probe beam will observe any anisotropy of the medium as a birefringence, due to diferential absorption of orthogonal components of the probe beam. This birefringence will be indicated by the rotation of the plane of polarisation. The rotation will be observed by an increase of intensity in one of the photodiodes analyzing the resolved components of the probe beam and a corresponding decrease in the other (see Fig. 3.8).

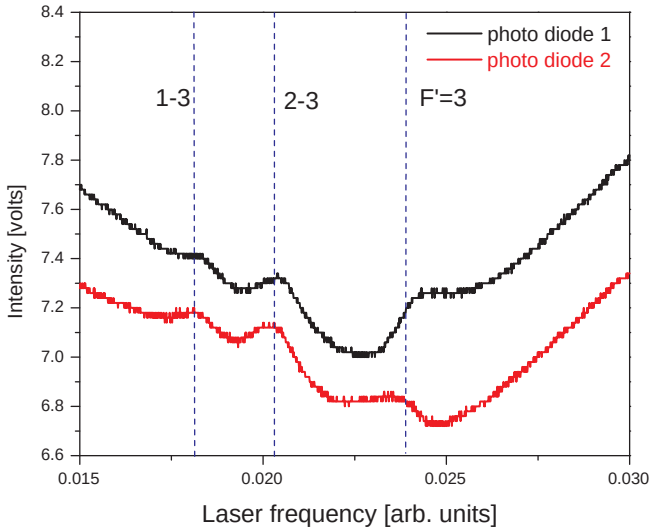

Figure 3.8: The signals collected by the two photodiodes located in our polarization spectroscopy setup. As written in the text, the rotation of the Probe's polarization plan is expressed by a decrease of the intensity on one diode and an increase on the other, at the transition frequency.

The error signal is produced by substracting one photodiode signal from the other using a differential amplifier. Optimization of the error signal can be achieved by the following measures:

- The overlap between the pump and probe beams along the atomic vapor has to be maximized. Under the limitation of space we managed to get a reasonable overlap indicated by a sharp error signal.

- The polarization angle should be aligned so that (in the absence of the pump beam) the intensity of the light reaching photodiode PD1 is equal to that reaching PD2 (see Fig. 3.7) .

- Polarization spectroscopy is very sensitive to external magnetic fields. To avoid those fields we wrapped our vapor cell with μ-metal shield. As a result, we obtain a signal which is more stable.

- Since the signal is sensitive to variations of pressure, we located the whole locking setup

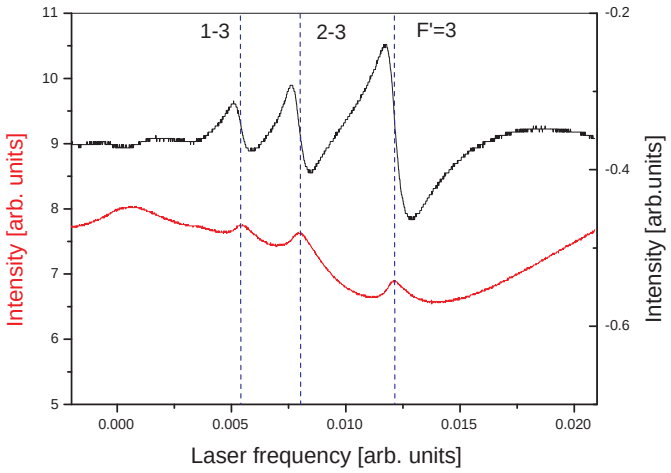

Figure 3.9: An error signal produced by polarization spectroscopy (black plot) and the results of the $F = 2 \rightarrow F'$ saturation spectroscopy (red plot)

in a P.V.C box, which is also useful for protecting the optical elements from dust, and enables work with the lights in the lab turned "on".

In Fig. 3.9, we see the error signal we obtained by polarization spectroscopy as well as the saturation spectroscopy results. To check the linewidth of our locked lasers, we beat them on a fast photodiode. The master is locked on the transition $F = 2 \rightarrow F' = 3$, while the probe is locked on the 1-3 crossover peak, and then blue shifted by 110 MHz, using an Acusto-Optic Modulator (AOM). Since the crossover peak is located 212 MHz away from the actual transition line, we get a beatnote at the frequency of $\sim$102 MHz (Fig. 3.10). The full width half maximum (FWHM) of that beatnote is estimated to be 750 KHz. Assuming that both lasers have similar though uncorrelated widths, we can estimate the single laser linewidth as about half of that.

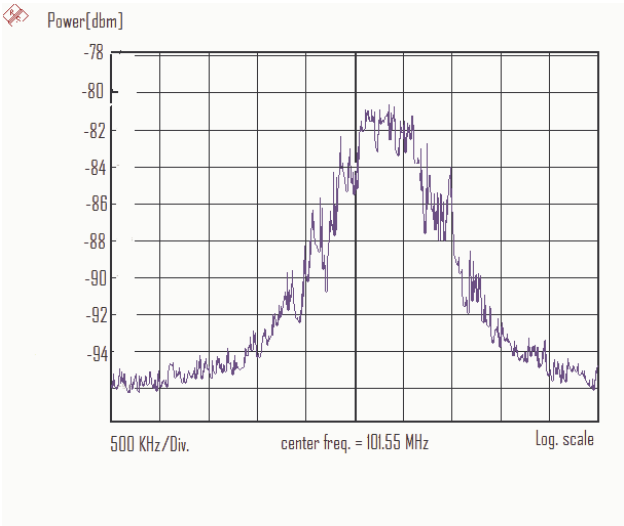

Figure 3.10: The beat note between the two locked lasers

3.3 The atomic medium

All the experiments described in this thesis were performed in a cylindrical pyrex cell of ∼12 cm^3 filled with Ne buffer gas and ^{87}Rb vapor. The diameter of the cell's quartz windows is 1 inch. The cell is located along the symmetry axis of a solenoid producing an external magnetic field. The earth's field is zeroed by a set of six compensation coils surrounding the cell (see Fig. 3.11).

The vapor pressure of ^{87}Rb in the cell at 25° C is 2×10^{-7} Torr [Ste01] leading to an atomic density $n \approx 10^{10}$ cm^{-3}. The pressure of the Ne is 7.5 Torr leading to an atomic density $n \approx 10^{17}$ cm^{-3}. The high density of the buffer gas prevents Rb-Rb collisions, which destroy coherence. Instead, the rubidium atoms collide frequently with the buffer gas atoms (With properly chosen buffer gas the ground-state coherence can survive more than 10^7 collisions without decay [Bra97]). In addition, the buffer gas prevents the rubidium atoms from propagating ballistically to the walls where collisional dephasing will occur. Instead they diffuse slowly throughout the cell, lengthening substantially the time during which they can interact with the excitation field.

A quantitive description for the relaxation induced by buffer gas collisions is given by the

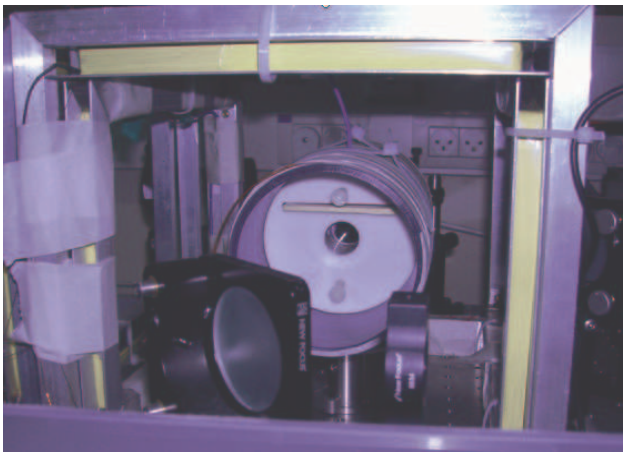

Figure 3.11: The atomic cell setup

ground state coherence rate [Bra98]:

$$\Gamma_{12} = AD_0\frac{p_0}{p} + N_0\bar{v}_r\sigma_2\frac{p}{p_0} \tag{3.5}$$

Where A is related to the geometry of the cell and D_0 is the diffusion constant at atmospheric pressure p_0 (760 Torr). N_0 is Loschmidts constant, $\bar{v}_r$ is the relative velocity of the rubidium and the buffer gas atoms and σ_2 is the decoherence cross-section, i.e. the cross-section for collisions producing a loss of coherence in the ensemble.

The first term in Eq. 3.5 is related to the diffusion of the atoms towards the walls and is dominant in low buffer gas pressures (a few Torr). The second term originates in collisions involving the formation of Rb-Ne bound states. Unlike the more frequent binary collisions, those collisions effect the internal state of the atom, therefore produce a loss of coherence. However, the second term is only dominant in high buffer gas pressures (hundreds of Torr). Since in our cell the buffer gas pressure is relatively low (7.5 Torr) we can neglect the second term. Substituting the parameters of our system into the first term we get an estimation for ground state coherence time: $\tau_{12} = 1/\Gamma_{12} \approx$7 ms. This value is about the same order of the experimentally measured coherence time.

Another effect induced by the buffer gas is the narrowing of the doppler broadened spectral line shape of the atomic ground state transition usually refered to as Dicke narrowing. In the presence of a few Torr of buffer gas we typically observe linewidths of about 300 Hz [Fru85] with only a small fraction of that due to the residual Doppler contribution, while

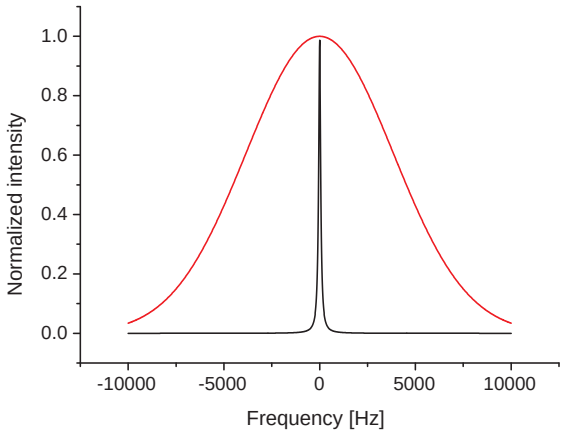

Figure 3.12: The effect of the buffer gas on the lineshape of the ground state hypefine transition is demonstrated by this graph. The doppler broadened gaussian profile (red plot) turns in the presence of buffer gas to a sharp lorentzian (black plot)

the full doppler width is ∼10 KHz (see Fig. 3.12). The major contributions to the linewidth arise from the effects of the optical pumping radiation, the microwave field, magnetic field gradients and the like. The lineshape derived by Dicke [Dic53] is given by

$$I(\omega) = \frac{(2\pi D/\lambda^2)}{(\omega - \omega_0)^2 + (2\pi D/\lambda^2)^2} \tag{3.6}$$

where λ is the wavelength of the transition. The full width at half maximum of the line is $2\pi D/\lambda^2$. For ^{87}Rb in 7.5 Torr Ne, we calculated a residual Doppler width, i.e. the Dicke-narrowed contribution, to be approximately 6 Hz.

3.4 The detection system

To induce and monitor population oscillations between the $F = 1$ and $F = 2$ hyperfine levels of the ^{87}Rb ground state, we apply the following basic sequence (see Fig. 3.13, the details of each step are presented later in this section):

- First, we prepare all the atoms in the $F = 1$ level, using a 100 μs probe laser pulse tuned to the $F = 2 \rightarrow F' = 3$ transition.
- We then send a radiation pulse (either microwave or laser) to the atomic sample.

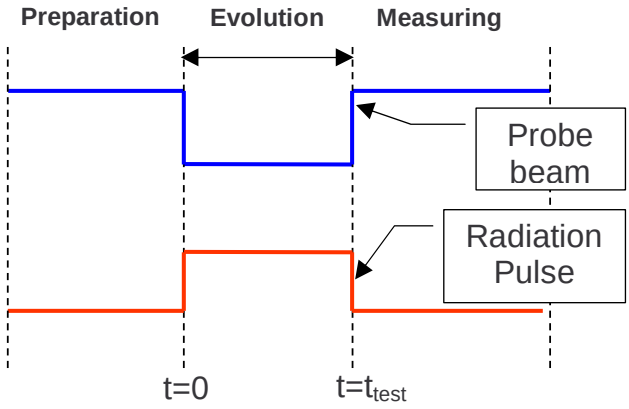

Figure 3.13: A diagram showing the experimental sequence

- We apply the probe laser pulse again (same duration and frequency) to detect the population in the $F = 2$ level.

This cycle is rerun several times, while the radiation pulse duration is increased each time. Our Labview program draws in real-time a graph of the population in $F = 2$ vs. the radiation pulse duration. We will now detail each step of the sequence:

Preparation- Although our probe beam is tuned to the $F = 2 \rightarrow F' = 3$ cyclic transition (atoms in $F' = 3$ can only decay to $F = 2$), some of the atoms will be excited to $F' = 2$ level, from where they can spontaneously decay to both $F = 1$ and $F = 2$ levels. As a result of this process, about once in a thousand such cycles, an atom will end up in the $F = 1$ level [Met99]. This atom is now trapped there, as there is no radiation tuned to excite it. Since the typical lifetime of atoms in the $5P_{3/2}$, is 26 ns, after 80-100 μs, all the populatoin will be trapped at $F = 1$. We set the preparation time in our sequence to be 100μs.

Radiation pulse- To be able to observe Rabi oscillations of the population in the ground state, we have to set the durations of the pulses, to match the expected Rabi frequency. Our system has a pulse resolution of 1μs, meaning we are capable of detecting Rabi frequency of up to $\sim$100 KHz.

Population measurements- The correlation between the intensity signal detected by the photodiode, and the population distribution is demonstrated in Fig. 3.14. The figure shows the variation of light intensity of the probe beam over time, for several cases. The saturation intensity (shown in Fig. 3.14), indicates all the atoms were pumped to $F = 1$. The intensity

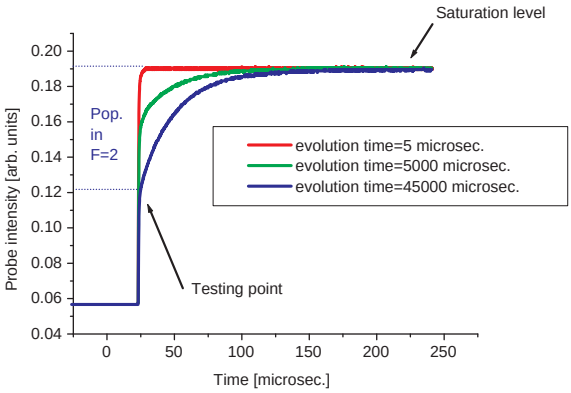

Figure 3.14: Several measurements of the probe intensity, for different evolution periods, are shown. The longer the evolution time is, the more population is transfered to $F = 2$.

level at the moment we turned on the probe beam ($t = t_{test}$) is correlated with the population level in $F = 2$. To find it, we fit the exponential decay function

$$I(t) = Ae^{-t/\tau} + B \tag{3.7}$$

to the measured decay of the probe beam absorption by the atomic sample. The intensity difference, $I_{sat} - I(t = t_{test})$, is proportional to the population in $F = 2$ at $t = t_{test}$.

3.4.1 Thermal relaxation

Assuming the Boltzman distribution, the ratio between the populations of two atomic states, in equilibrium, is given by

$$\frac{P_2}{P_1} = e^{-(h\nu/K_bT)} \tag{3.8}$$

where ν corresponds to the energy difference between the two states. Introducing a frequency corresponding to the energy of the first excited state of ^{87}Rb, we get $\frac{P_2}{P_1} \approx 10^{-25}$, meaning all the population is concentrated in the two hyperfine levels of the ground state.
Although Eq. 3.8 predicts equal populating of the two hyperfine levels ($\frac{P_2}{P_1} = 0.9989$), due to different degenerecies (3 for $F = 1$ and 5 for $F = 2$), they are not equally populated, but conatain the following fractions of the total number of atoms:

$$\begin{aligned} f_1 &= \tfrac{3}{3+5} = \tfrac{3}{8}, \\ f_2 &= \tfrac{5}{3+5} = \tfrac{5}{8}. \end{aligned} \tag{3.9}$$

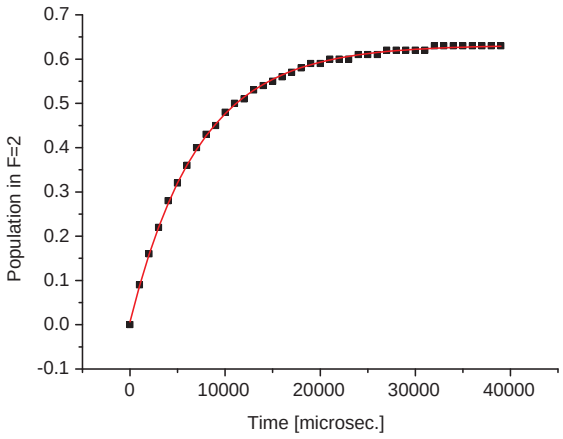

Figure 3.15: The thermal relaxation of the atomic population is shown. From the fit we extracted the thermal relaxation time constant $\tau = 8172\mu$s.

The thermal relaxation process, will thus bring an atomic ensemble, initially prepared in the $F = 1$ level, to a mixed state, with 62.5% of the population at $F = 2$. To monitor that thermal relaxation, we prepare all the atoms in $F = 1$ using our probe laser, then let them evolve in the dark, and then measure the populations, again by our probe light. Applying this sequence for different "evolution periods" varying from several microseconds to several milliseconds, we get the time evolution described in Fig. 3.15. The ploted data is fitted to

$$P_2 = A(1 - e^{-t/\tau}). \tag{3.10}$$

The constant τ, calculated from that fit, is basically the longitudinal coherence time T_1, defined in Sect. 2.1.5. The observation of Rabi oscillations due to external coupling of the hyperfine levels is possible only at $t < \tau$ before thermal behavior takes over. In our system, we measured, τ=8.172 ms. Since we expect Rabi oscillations of several KHz, we will be able to observe some oscillation periods, before the system decoheres.

Chapter 4

Rabi oscillations in the microwave field

4.1 Experimental setup

The system setup for monitoring the direct interaction of the ^{87}Rb atom with microwave radiation is described in Fig. 4.1. The microwave pulse is transmitted from the signal generator to the rubidium cell through a flat microwave antenna located about 5 mm above the cell. The antenna is made of a 50×50 mm square PCB, with a front (transmitting) 10×10 mm copper square printed on one side, while the back (ground) side is all copper. We measured the magnetic field transmitted by this antenna along the length of the vapor cell, and found that while the field was quite constant through about 2/3 of the cell length, it drops by a factor of 3 towards the edge of the cell. As a result we expected that part of the ^{87}Rb population will oscillate at a slower Rabi frequency, leading to attenuation of the oscillation amplitude with time.

The electromagnetic wave transmitted by the antenna is linearly polarized and propagates in the direction of the x axis (Fig. 4.2). The induced electric and magnetic fields will thus have perpendicular components in the YZ plane. We can control the exact direction of those components by just rotating the antenna in the YZ plane. In most of the experiments we positioned the antenna so as the magnetic field will oscilate in the direction of the z axis, parallel to the direction of the constant field.

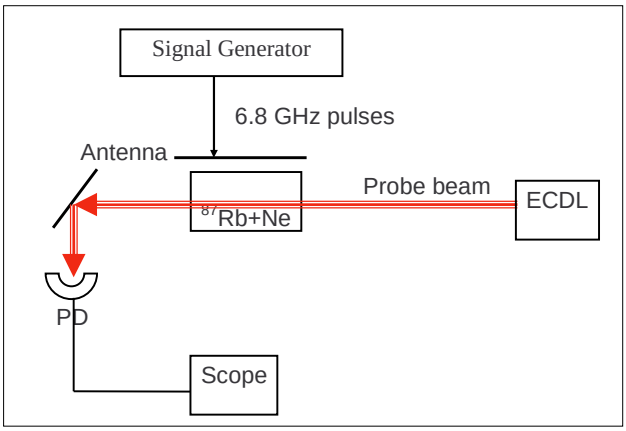

Figure 4.1: The system setup

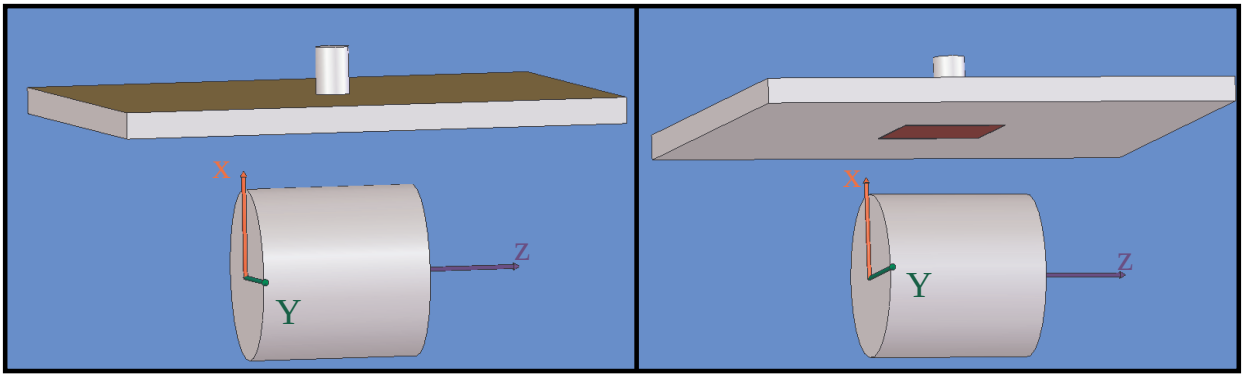

Figure 4.2: This figure shows the position of the anntena in relative to the atomic vapor cell

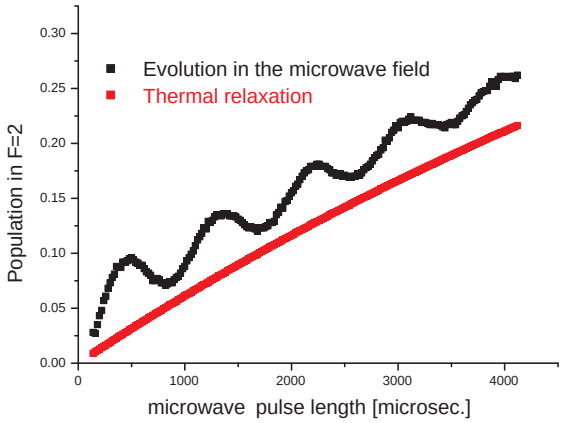

Figure 4.3: The graph of the population in $F = 2$ as a function of the pulse length (black plot), comparing to the thermal relaxation (red plot)

4.2 Results

The evolution of the population of the $F = 2$ level as a result from the interaction with the microwave radiation is described in Fig. 4.3 by the black plot. Subtracting from it the evolution of the population of the $F = 2$ level under thermal relaxation (the red plot), we get a plot of Rabi oscillations of the atomic population in $F = 2$ hyperfine level of the ^{87}Rb ground state (Fig. 4.4). We then fit the data points to an exponentially decaying cosine:

$$f(t) = Ae^{-t/t_0}\cos(Wt + \varphi) + B \tag{4.1}$$

W and t_0 are our estimations for the generalized Rabi frequency (or the flopping frequency) and the decay time of the oscillations respectively. In the example shown in Fig. 4.4 the flopping frequency and the decay time were found to be $\bar{\Omega} = 2\pi\cdot 1{,}143\pm 3.18$ Hz and t_0=3,817$\pm$192 μs.

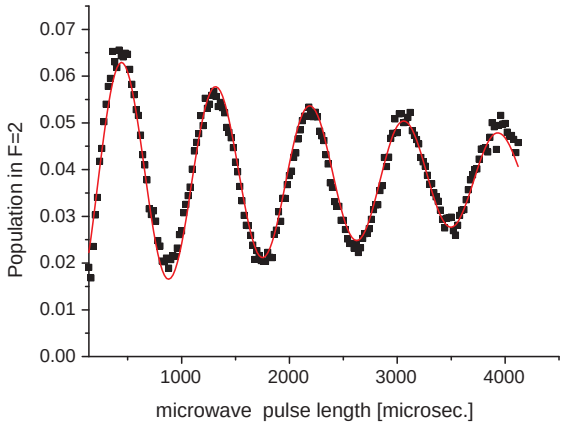

Figure 4.4: The plot shows data collected in a measurement of Rabi oscillations. The curve is a fit to an exponential decaying cosine

4.2.1 The dependency of Rabi oscillations on the field frequency

The relation between the generalized Rabi frequency and the microwave field frequency ω is given by

$$\bar{\Omega} = \sqrt{\Omega^2 + (\omega - \omega_0)^2}. \tag{4.2}$$

To verify this relation we kept the output power of the signal generator at a constant level of 0 dbm and varied the output frequency. For each value of frequency we got an oscillations graph from which we extracted the flopping frequency. The results were summarized in a graph (Fig. 4.5). The data plot is fitted to Eq. 4.2. The minimum point of the curve corresponds to the resonance frequency, which in our case is determined to be $\omega_0 = 2\pi\cdot$6,834,686,146$\pm$12.17 Hz. The $\sim$3.5 KHz shift from the rubidium ground state's hyperfine splitting value ($\Delta_{HFS} = 2\pi\cdot$6,834,682,610 Hz) is induced by the interaction with the buffer gas atoms [Hap72].

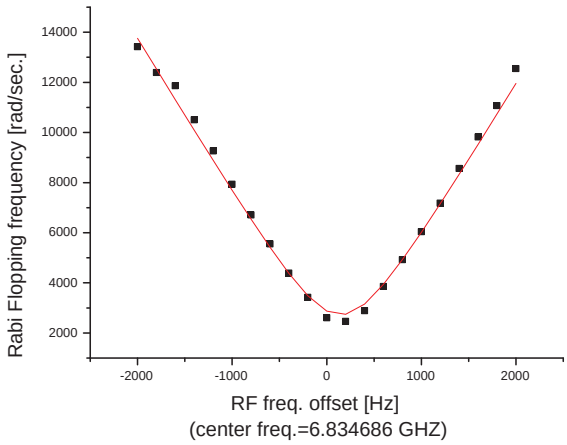

Figure 4.5: Plot of the generalized Rabi frequency versus the frequency of the microwave field. The data points have been fitted to Eq. (4.10). The values of the Rabi frequency and the resonance frequency were found to be $\Omega = 2\pi{\cdot}433{\pm}10.9$ Hz and $\omega_0 = 2\pi{\cdot}6{,}834{,}686{,}146{\pm}12.17$ Hz The corresponding uncertainties for the generalized Rabi frequencies have been omitted since they are very small.

4.2.2 The dependency of Rabi oscillations on the field power

To test the relation between the field amplitude and the oscillations frequency, we preformed the following experiment. The generalized Rabi frequency was measured several times, each time for a different output level of the microwave generator. The power was changed between -11 to +11 dbm with 1 dbm interval. The experiment was preformed twice for 2 different field frequencies. First, with microwave radiation at the resonance frequency (which was found in the experiment described in the previous section) and then for a $\sim 500Hz$ blue detuned frequency.

It is known that the energy flow of an electromagnetic wave is given by the magnitude of Poynting vector:

$$|\mathbf{S}| = \frac{1}{\mu_0}|\mathbf{E}\times\mathbf{B}| = \frac{1}{2}\frac{c}{\mu_0}{B_1}^2 \tag{4.3}$$

where we have averaged over an entire period of oscillation. The Rabi frequency, by its definition, is linear with the magnetic field B_1, therefore $\Omega \propto \sqrt{|\mathbf{S}|}$. Assuming $\mathbf{S}$ is proportional to the output power of our signal generator, we may write, for the generalized Rabi

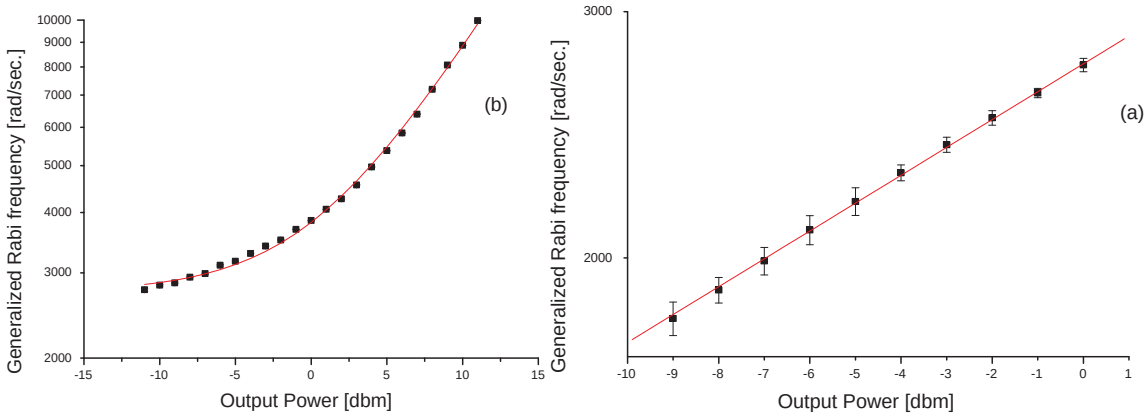

Figure 4.6: A logarithmic plot of the power output vs. the generalized Rabi frequency. In (a) The field frequency was tuned to resonance ($\omega = 2\pi{\cdot}6.834686150$ GHz) and the data fitted to a linear curve. In (b) the field is blue detuned by 500 Hz and data is fit to Eeq. 4.4.

frequency,

$$\bar{\Omega} = \sqrt{C \cdot 10^{P[dbm]/10} + (\omega - \omega_0)^2}. \tag{4.4}$$

where C is some constant and the power is expressed in dbm for convenience. Close to resonance, we may neglect the second term under the square root to get a linear dependency between the logarithm of the power and the flopping frequency. In Fig. 4.6 we show the results for both the resonant (Fig. a) and the off resonant (Fig. b) cases. The logarithmic plot on (a) was perfectly fitted to a linear curve, while the plot on (b) was fitted to Eq. (4.4). The detuning calculated from the fit is $2\pi{\cdot}436{\pm}4.23$ Hz.

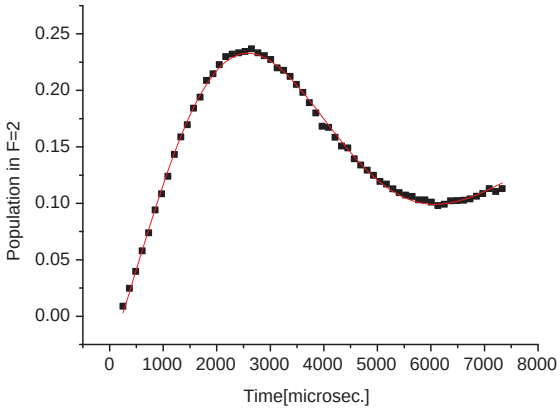

Figure 4.7: The Rabi oscillations graph with a 0.6 G bias field. The microwave frequency in that measurement was set to be 6.834686660 GHz. The Rabi frequency of the oscillations is calculated from the fit to be $\bar{\Omega} = 2\pi \cdot 143.4 \pm 2.1$ Hz.

4.2.3 Oscillations in an external constant magnetic field

To check the behavior of the atomic system in the presence of an external constant magnetic field we preformed the following experiment. We zeroed the ambient magnetic fields with our compensation coils, turned on an external magnetic field along the z-axis, and preformed the sequence to get Rabi oscillations. We executed some measurements for different field magnitudes between 0 and 1 G. In Fig. 4.7 we show oscillations graph obtained when applying a 0.6 G bias field. The Rabi frequency of the oscillations is reduced in the presence of the external field: In the absence of the constant field, we measured a Rabi frequency of 340 Hz on resonance, while in a 0.6 G field the Rabi frequency is 143 Hz. The first order Zeeman shift of all sublevels but $m_F = 0$ leads to the reduction of the total magnetic dipole matrix element and of the Rabi frequency accordingly.

Note: The Zeeman splittings between adjacent magnetic sublevels of ^{87}Rb is 0.7 MHz/G [Ste01]. In a 0.6 G field we thus expect a first order Zeeman shift of $\Delta\nu = n \cdot 420$ KHz for the various transitions between Zeeman sublevels (except the transition between $m_F = 0$ sublevels), where $n = 1, 2, 3$ (see a diagram of the possible transitions in a magnetic field and their energies in appendix B). This shift is by several orders of magnitude larger than the transition linewidth (see Sect. 3.3)

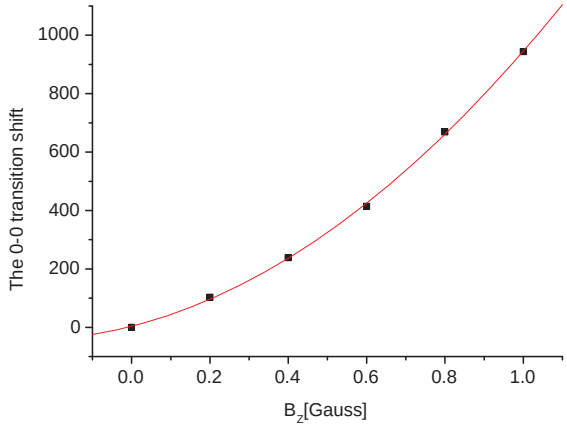

Figure 4.8: The clock transition shift versus the external magnetic field. The data is fitted to a parabolic curve

In second order of the magnetic field, the shift of the transition between the $m_F = 0$ sublevels ("clock transition") is given by:

$$\Delta\omega_{clock} = \frac{(g_J - g_I)^2 {\mu_B}^2}{2\hbar\Delta E_{hfs}} B^2. \tag{4.5}$$

We scanned over the microwave frequency to detect the variation of the resonance transition frequency due to the external field. The results are shown in Fig. 4.8. The data collected are fitted to a second-order polynomial. The second-order Zeeman shift, calculated from the fit parameters ($\Delta\omega_{clock} = 2\pi{\cdot}598.23{\pm}12.67$ Hz/G^2) is in good agreement with the value calculated via Eq. 4.5 ($2\pi{\cdot}575$ Hz/G^2).

4.3 Oscillation decay

In the previous section we demonstrated population oscillations of a two-level atom subjected to microwave radiation. The measurements of those oscillations were made on an atomic ensemble consisting of $\sim 10^{10}$ ^{87}Rb atoms. This means that the Rabi oscillation graph (see Fig. 4.4) is an average over single-atom oscillation graphs, and the generalized Rabi frequency calculated is an average over single-atom frequencies. Due to several effects, different atoms in the ensemble will oscillate with a different frequency leading to a decay of the Rabi oscillations.

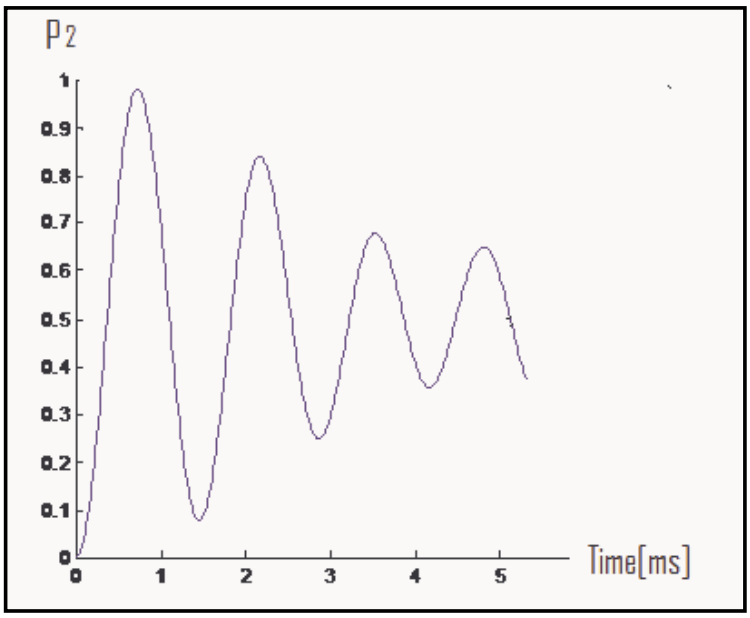

Figure 4.9: The results of a simulation of Rabi ooscillations in an inhomogeneous field.

Since we use a buffered cell, the effect of both doppler and collisions broadening on the Rabi oscillations amplitude can be neglected (The buffer gas effect is detailed in Sect. 3.3). The decay of the oscillations is mainly related to an inhomogeneous field distribution along the atomic sample.

We measured the induced microwave power in the atomic cell, and found out it is attenuated along the main axis (z-axis):

$$p(z)[dbm] = p_0(1 - 0.00175z^2). \tag{4.6}$$

The maximal intensity (p_0) is at the cell center (z=0). Substituting 4.6 into 4.4 we get the dependency of the Rabi frequency in the atom's location

$$\bar{\Omega}(z) = \sqrt{C \cdot 10^{\frac{(1-0.00175z^2)p_0}{10}} + \delta^2} \tag{4.7}$$

followed by the probability to find the atom in the $F = 2$ level

$$P_2(z) = \frac{1}{2}\frac{\Omega(z)}{\bar{\Omega}(z)} + \left[1 - \cos(\bar{\Omega}(z))\right]. \tag{4.8}$$

Using this formula we can simulate the population evolution of our atomic ensemble consisting of 10^{10} atoms. Each one of the atoms oscilates in a different generalized Rabi frequency which depends on its location. The addition of single atom oscillations curves with different

oscillation frequencies results in the decay of the Rabi oscillations of the entire ensemble, as is shown in Fig. 4.9. The decay time of the Rabi oscillations was calculated to be 4.63 ms, which is in good agreement with the experimental results.

Chapter 5

The Raman laser system

5.1 Generation of the Raman beams

To drive the two-photon transition between the rubidium hyperfine ground state levels $F = 1$ and $F = 2$, two Raman beams are needed fulfilling the following requirements:

- The frequency difference of the Raman beams has to match the hyperfine splitting of the ^{87}Rb ground state (6.8 GHz)
- The two beams have to be phase locked
- The frequency difference has to be scanned over a range of a few MHz with less than a Hz resolution and a similar absolute frequency accuracy has to be provided.
- The Raman beams have to be several GHz detuned from the one-photon resonance, to minimize spontaneous emission.
- The power of the Raman laser beams has to be reasonably stable to avoid fluctuations of the Rabi frequency during the coherent manipulation of the atom.
- The Raman beams have to be spatially separated, so we can control their polarizations separately.

There are three main ways to create the Raman beams:

- Phase locking of two separate lasers [Sch96]

- Modulating the light of a laser, using AOM [Bou96] or EOM [Sha00].
- Modulating the current of a diode laser [Rin99]

In our experiment we use the third method to create optical sidebands at ±3.4 GHz. Each side band is injected to a slave laser for amplification.

5.1.1 Current modulation of a diode Laser

A laser diode injected by a pure DC current will produce an almost monochromatic light field. This field can be written as

$$E = E_0 e^{i\omega t}. \tag{5.1}$$

Modulating the current injected to the diode with a sinus wave will induce a phase to that field namely

$$E = E_0 e^{i\omega t + m\sin(\Omega t)} \tag{5.2}$$

where m is the modulation index and Ω is the modulation frequency. Expanding eq. 5.2, using Fourier components will lead to

$$E = E_0 \left(\sum_{k=0}^{\infty} J_k(m) e^{ik\Omega t} + \sum_{k=0}^{\infty} (-1)^k J_k(m) e^{-ik\Omega t} \right) e^{i\omega t} \tag{5.3}$$

where J_k, the bessel function from the order k, represents the amplitude of the $k-th$ sideband. In particular, J_0 is the amplitude of the carrier (the component with the unmodulated frequency). The typical value of m, in our experiments, is smaller than one. In that regime, J_0 is the dominant component (see Fig. 5.1). When we increase m the amplitude of J_0 decays while the sidebands' amplitudes increase. At $m = 2.4$ the carrier is completely suppressed. To modulate the diode's current we have used a $Rhode - Schwartz\ SMR - 20$ Signal Generator locked to an $Accubeat\ AR40A$ atomic clock reference. The maximum power available is 100 mw. The output microwave signal is fed to a $MiniCircuit$ Bias tee via a directional coupler. In the Bias tee the microwave is combined with the laser diode's DC injection current. This combined signal is then fed to the laser diode via an impedance matching circuit. The reflected signal (available at the reflecting port of the directional

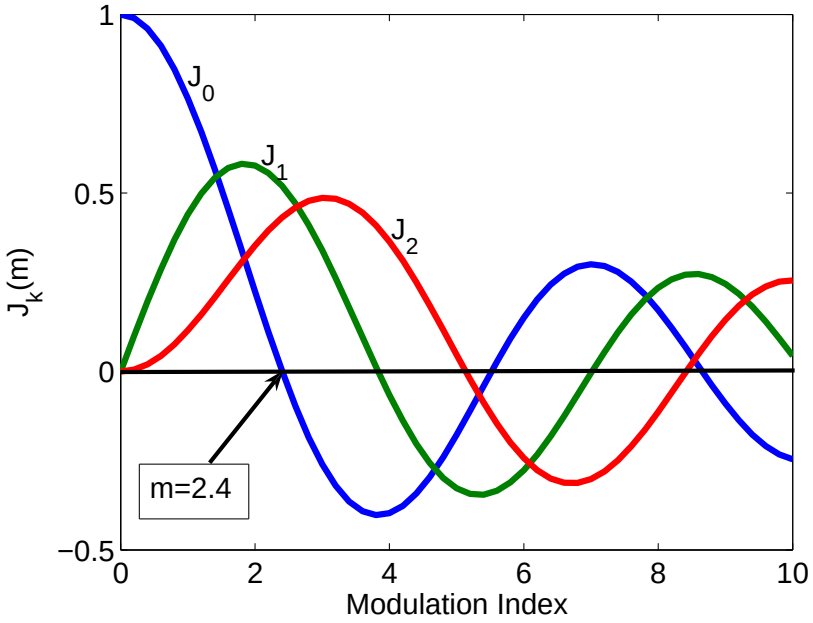

Figure 5.1: The first three orders of the Bessel functions representing the relative amplitudes of the carrier and the sidebands.

coupler) can be monitored on our $Rhode-Schwartz\ FSP13$ Spectrum Analyzer, to indicate the degree of the modulation efficiency.

The extended cavity length has a major effect on the modulation depth [Rin99]. The cavity length thus has to be modified according to the modulation frequency. We scanned the laser's cavity length ,L, for the best modulation responce at the relevant frequency (3.4 GHz), and found that at L≈3 cm the modulation responce is optimized.

Further optimization of the modulation depth can be made by tuning the injection current. This tuning is carried out when the master laser is modulated and locked to it's reference atomic transition (The tuning amplitude is below 0.2 mA variation, so as not to change the frequency too much). This tuning operation can significantly increase the sidebands' intensity.

The modulation induced ±1 sidebands are shown in Fig. 5.2. The spectrum was obtained by a scanning Fabry Perot $Toptica\ FP$ 100 01047. The amplitude of each side band is approximately 5% of the carrier's.

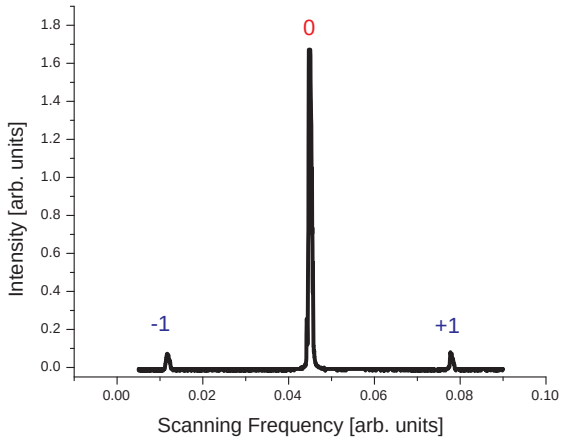

Figure 5.2: The FP scan of the modulated light. The two little peaks on the sides represent the generated sidebands, while the central peak represents the carrier frequency.

5.1.2 Slave seeding (injection)

Seeding a laser diode (slave laser) with a low power signal from another laser may lock the slave's light frequency and phase to that of the seeding light. In this way we can amplify a light signal without increasing the bandwidth. Since the sidebands obtained by the modulation are of low power (∼500 μw), we seed them into laser diodes with a maximum output power of 100 mw. The injection setup is shown in Fig. 5.3.

Accurate mode matching between the master and the slave is essential to the success of the injection. Mode matching requires accurate alignment of the seeding beam (= beam entering the slave laser) and seeded beam (= beam leaving the slave laser). This alignment is done by checking the overlap of both beams on the surface of the three mirror located on the long master beam's trajectory (see Fig. 5.3). We also match the beams polarizations, using a $\lambda/2$ plate placed in front of each slave.

We use one sided AR coated windows to reflect the seeding beam into the slave. Only a small fraction of the master light is used to inject the slaves. In our experiments we did not exceed the seeding power of 200 μw, so as not to burn the slave laser's diodes.

Each slave can be locked on the desired side-band by adjusting its gain curve through the injection current. Seeding will occur when the emission frequency of the slave laser is close enough to the master's frequency. The size of the "injection window" follows the relation

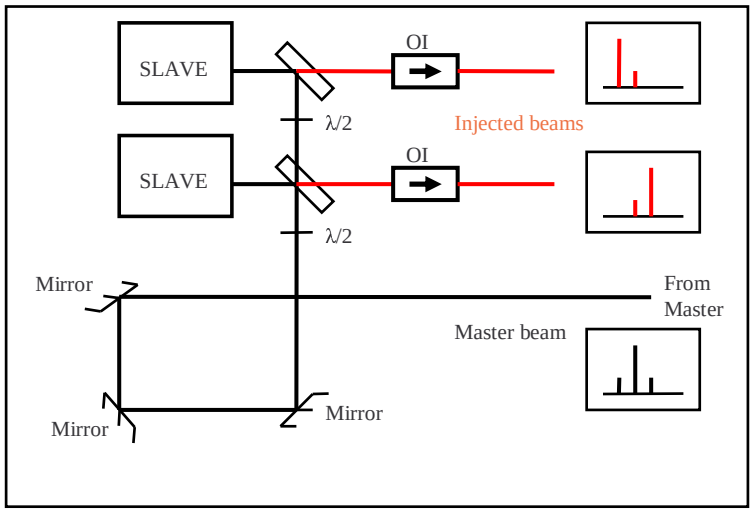

Figure 5.3: The injection setup is shown. In the small squares the spectral difference between the injected slave beams (red) and the master beam (black) is visualized. The alignment is done by checking the overlap of both seeding (master) and seeded (slave) beams on the surface of the three mirror located on the long master beam's trajectory

$\Delta\nu \propto \frac{I_{master}}{I_{slave}}$. This frequencies window should not be too large, since we want to avoid the injection of the carrier and the other sideband.

It is possible to switch the locked sideband, by varying the current within ∼5.5 mA (this number relates, of course, to our lasers). For convenience, we prefer to constantly lock one slave to the -1 sideband (Stokes beam), and the other to the $+1$ sideband (pump beam). While tuning the current to inject each sideband, we look at the beam spectral profile, analyzed by the Fabry Perot. The moment the seeding occurs the peak gets much narrower and steadier (see Fig. 5.4).

Figure 5.5 shows the frequency analysis of the two injected slaves. Note that we still have remains of the carrier light in the spectral profile. This is due to the fact the intensity of the carrier component in the master beam is much higher than the sidebands intensity. The "injection window" for the carrier frequency is therefore much wider. To filter the remains of the carrier, a Mach-Zender interferometer can be used [Hau00].

We beat the two phase locked slaves, on a *EOT ET* − 4000 fast Photodiode . The resulting beat note (received on the Spectrum Analyzer) is shown in Fig. 5.6. Its FWHM was measured to be 1.2 Hz. Such a narrow beat note from two ∼20 MHz width lasers, is only

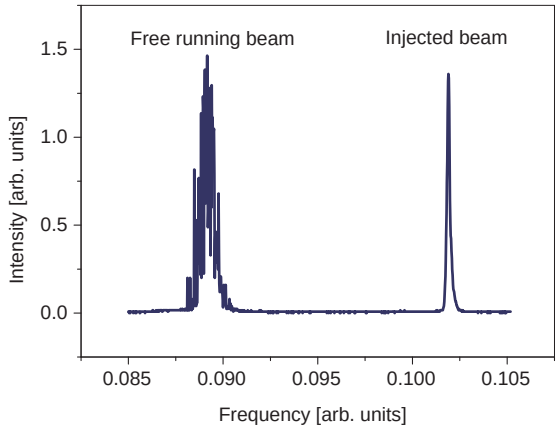

Figure 5.4: A comparison between a free running beam (on the left) and injected beam. The linewidth of the beam on the left is estimated to be 30 MHz, while the beam on the right is estimated to be narrower than 1 MHz (the resolution limit of the FP is 4 MHz).

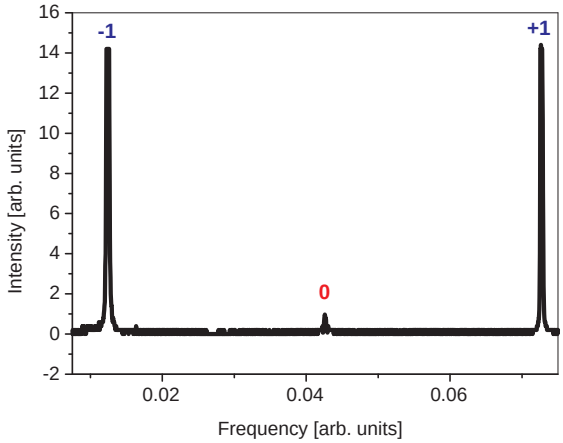

Figure 5.5: The spectral profile of the injected slave lasers.

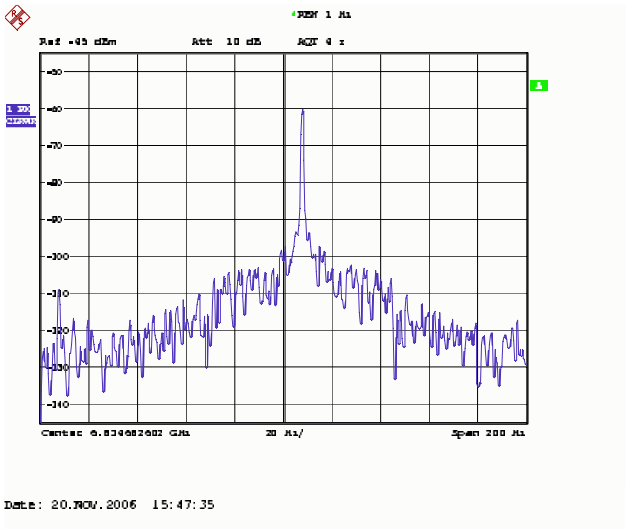

Figure 5.6: The beat note recorded between the two phase locked slaves. The x-axis scale is 20 Hz/square and the y-axis scale is logarithmic. The center frequency is 6.834682602 GHz.

possible if they are phase locked.

The output of the setup described in this section, is two phase locked Raman beams with tunable (to within 1 Hz) frequency difference in the range of 6.8 GHz.

5.2 Experimental setup

The system we built to stimulate and detect the Raman transitions is described in Fig. 5.7. After we modulate the master laser by a 3.4 GHz signal, we lock the carrier frequency on the atomic transition $F = 2 \rightarrow F' = 3$. As a consequence the detuning of the Raman beams from the excited state will be $\Delta \approx 3$ GHz. This is visualized by the diagram in Fig. 5.8. Since the Raman beams are far detuned from the atomic transition, it is possible to work with free running lasers in case the beams are not injected to slaves [Dot02]. We had to lock our master laser or its drift will "unseed" the slave laser within a few minutes.

Next, we tune the slave lasers current to inject each one of them by a different sideband. The two phase locked injected Raman beams (red beams in Fig. 5.7) are combined by a 50/50 Beamsplitter. Half of the power is sent to the experiment while the other half is sent to analysis (on FP and Spectrum Analyzer).

The pulsing of the light is made by placing an AOM in the optical path. The AOM can

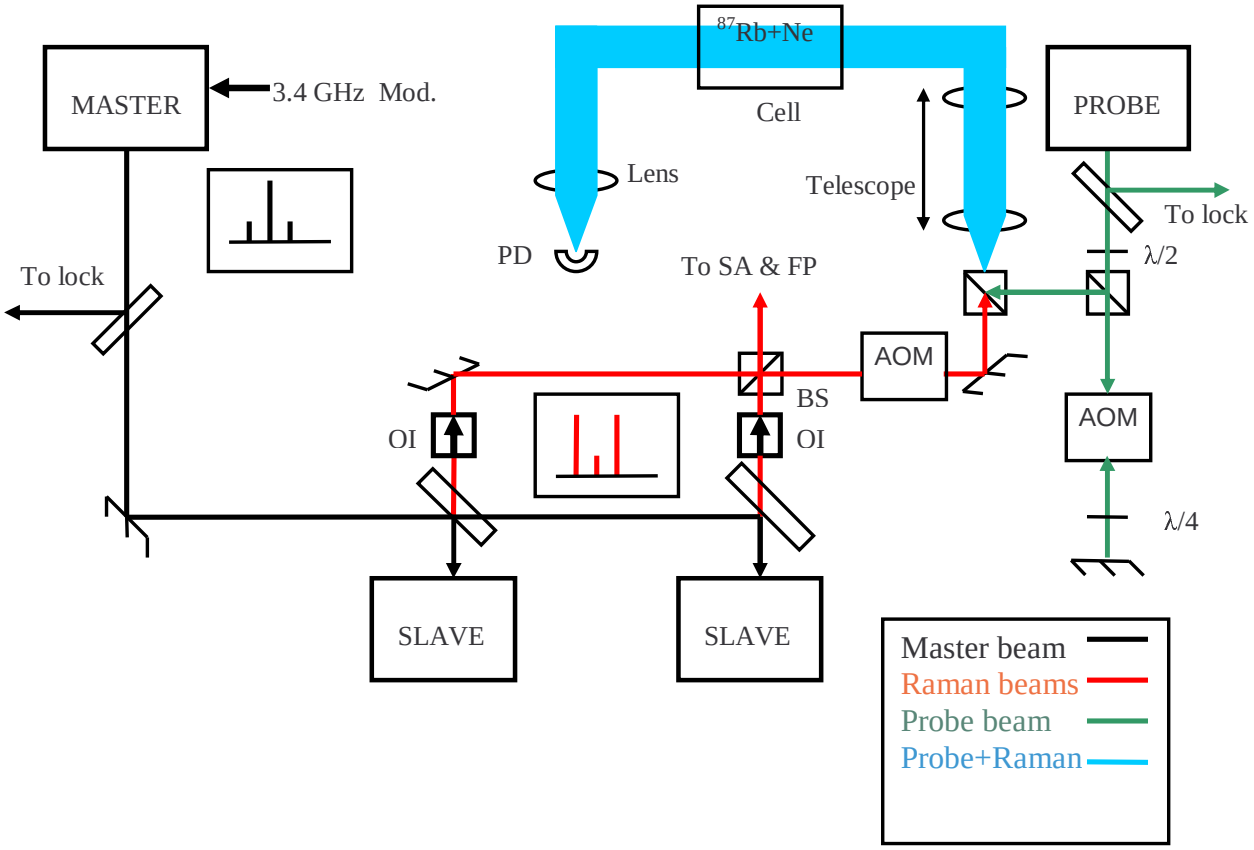

Figure 5.7: The layout of the Raman system

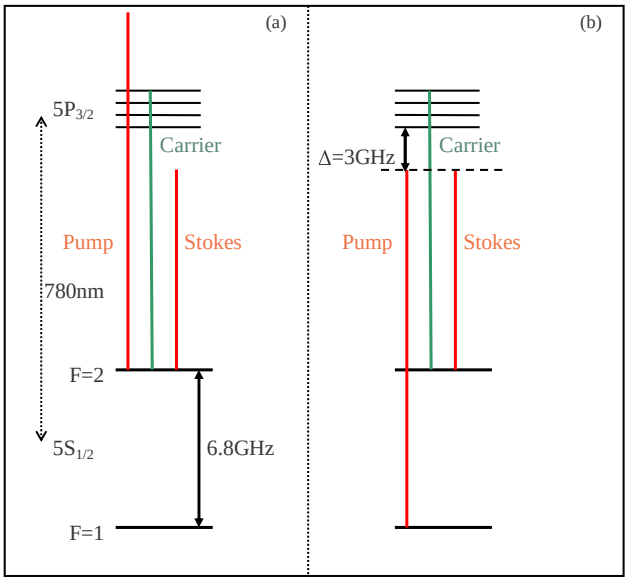

Figure 5.8: As written in the text, we lock the carrier frequency (green line) on the $F = 2 \rightarrow F' = 3$ transition. The pump and Stokes (red lines) will gain higher and lower frequency, respectively (a). Taking the pump beam to couple the $F = 1$ state and the excited state (b), we get a Λ system, detuned by $\sim$3 GHz from the excited state.

serve as a high speed switch due to its 1 nanosecond response time. We used a *Crystal − Technologies* AOM with a fixed frequency shift of 80 MHz. We used the +1 order of the modulated light, shifting the Raman beams to the blue.

The probe laser beam is locked on the 1-3 crossover peak which is red detuned by 212 MHz from the $F = 2 \rightarrow F' = 3$ transition. The beam then double passes through another AOM which is tuned to shift the beam by 106 MHz. We use the +1 diffracted order, twice, so as the outcoming beam is tuned to the atomic transition. The probe and the Raman beams are then combined through another 50/50 beamsplitter, and then the beam's waist in increased using two lenses in a telescope configuration. The wide beam is sent to the ^{87}Rb vapor cell. We devoted much attention to align the two Raman beams parallel to each other, to decrease doppler broadening. An atom with a velocity v will absorb light of different frequency from the resonance frequency ω_0, namely

$$\omega_a = \omega_0 - \mathbf{k} \cdot \mathbf{v}. \tag{5.4}$$

The doppler shift of the two-photon Raman transition is thus

$$\delta_{doppler} = (\omega_{pa} - \omega_{sa}) - (\omega_p - \omega_s) = \mathbf{v} \cdot (\mathbf{k_p} - \mathbf{k_s}) \tag{5.5}$$

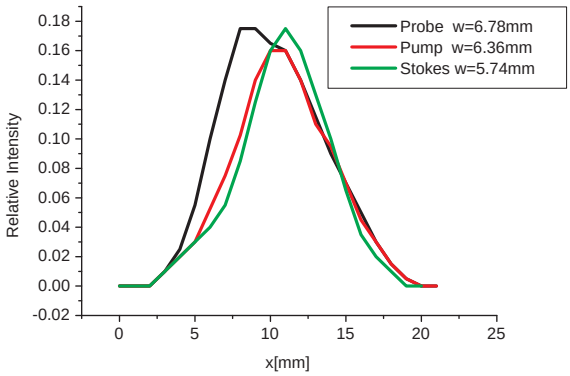

Figure 5.9: The Intensity profile along the x-axis of all three beams are compared. The beams' waists are noted. Similar profiles were recieved in a measurement along the y-axis.

where ω_{pa}, $\mathbf{k_p}$ and ω_{sa}, $\mathbf{k_s}$ are the doppler shifted angular frequency, and the k-vector, of the pump and Stokes beams respectively. It is clear from Eq. 5.5 that the minimal shift is achieved when the beams are copropagating. For copropagating beams and an atom moving in its most probable velocity (240 m/sec for ^{87}Rb), we calculated a doppler shift of $2\pi\cdot 5.45$ KHz. A deviation of 10 mm between the beams centers over 1 meter distance (corresponding to an angle of 10 mrad between the beams) will lead to a doppler shift of $\sim$95 KHz (at the most probable velocity). In the presence of buffer gas, however, the doppler broadening is greatly reduced due to Dicke narrowing (see Sect. 3.3).

The overlap of the Raman beams is verified by measuring their intensity profile in the interaction area. The gaussian profile of the beams is shown in Fig. 5.9. In most of the measurements we used circularly polarized Raman beams (both of the beams are either σ^+ or σ^- polarized), to stimulate $\Delta m_F = 0$ transitions. Alternatively, one of the beams can be π polarized, to induce $\Delta m_F = 1$ transitions. Two π polarized beams will lead to zero amplitude of the transition (see Sect. 2.2).

5.3 Coherent and noncoherent results

The theoretical analysis predicts that Raman beams (whose frequency difference is tuned to the ground-level hyperfine splitting) will induce Rabi population oscillations between those

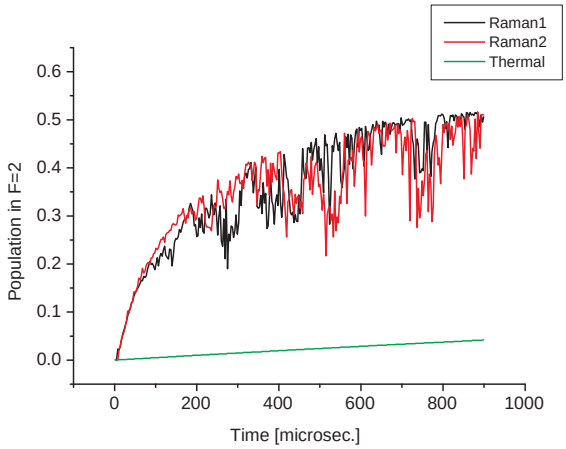

Figure 5.10: The Population evolution during the interaction with the Raman beams. The results of two measurements are plotted. The thermal relaxation is plotted for reference.

two sublevels (see Sect. 2.2). A typical result is presented in Fig. 5.10. For reference, the thermal relaxation curve is also shown on the same axes. We note first a sharp increase in the population at $F = 2$ level (much steeper than the thermal relaxation curve), followed by rapid and irregular population fluctuations. In the following section we suggest an explanation for this behavior.

5.3.1 Rate equations

Our first step will be to find the time dependence of the population P_2 in $F = 2$. Then we will examine the change of that time depndence under interaction with the Raman laser field.

The time dependence of the excited state population in our two level system obeys the following first order differential equation:

$$\frac{dP_2(t)}{dt} = P_1(t) \times R_{1\to 2} - P_2(t) \times R_{2\to 1} = (1 - P_2(t)) \times R_{1\to 2} - P_2(t) \times R_{2\to 1} \tag{5.6}$$

where $R_{1\to 2}$ and $R_{2\to 1}$ are the transfer rates of population from levels $F = 1$ and $F = 2$ respectively. The solution is an exponential function of the form

$$P_2(t) = \frac{R_{1\to 2}}{R_{1\to 2} + R_{2\to 1}} + C \cdot e^{-(R_{1\to 2}+R_{2\to 1})t}. \tag{5.7}$$

The integration constant C is calculated from the initial condition $P_2(t=0)=0$ to give

$$P_2(t) = \frac{R_{1\to 2}}{R_{1\to 2}+R_{2\to 1}} \times (1 - e^{-(R_{1\to 2}+R_{2\to 1})t}) \tag{5.8}$$

Substituting $P_1(0)=1$, $P2(0)=0$ in Eq. 5.6 we get

$$\frac{dP_2(0)}{dt} = R_{1\to 2}, \tag{5.9}$$

while the equilibrium condition, $\frac{dP_2(t)}{dt}=0$, leads to

$$P_{1Eq} \times R_{1\to 2} = P_{2Eq} \times R_{2\to 1}. \tag{5.10}$$

Using 5.9, 5.10 and our experimental results (see Fig. 3.15),the transition rates due to thermal relaxation calculated for our atomic sample are: $R_{1\to 2}$=76.50 Hz, $R_{2\to 1}$=45.90 Hz.

5.3.2 The affect of the carrier

Another non coherent process affecting the population in our two-level system is scattering (=excitation and spontaneous emission) caused by the laser beams. Due to the way we generate our Raman beams (see Sect. 5.1), there is still a component of the carrier frequency in each Raman beam. Being tuned close to resonance (of the $F=2 \to F'=3$ transition), this component has a large affect on the scattering rate. In a series of measurements with a beam at the carrier frequency only, we tested the influence of that beam on the population in $F=2$. The results are shown in Fig. 5.11. The different curves represent different intensities and detunings of the laser beams. From the fit of the data to the function

$$P_2 = A(1 - e^{-t/\tau}); \quad 1/\tau = R_{1\to 2} + R_{2\to 1} \tag{5.11}$$

we can calculate the population transition rates. The results are summarized in table 5.1 (the first column, test 1, is the thermal relaxation reference). The last two rows of the table (highlighted) show the effect of carrier excitation, after subtracting the thermal relaxation results. Note that the excitation rate from $F=2$ keeps the relation $\Delta R_{2\to 1} \propto I/\Delta^2$ which is in good agreement with scattering theory (see Sect. 2.2.3).

From the graph and the table we can conclude that:

First, the carrier frequency has almost no effect on the initial slope of the population curve,

beam properties	test 1	test 2	test 3	test 4	test 5	test 6
$\Delta[MHz]$	No light	80	80	1100	1100	1100
Power[mw]	No light	0.007	0.0015	0.76	0.21	0.006
A	0.63	0.25	0.5	0.26	0.45	0.63
$\tau[\mu s]$	8300	4500	7300	3000	6000	8300
$R_{1\to2}[Hz]$	75.9	51.1	68.5	86.7	75.0	75.9
$R_{2\to1}[Hz]$	44.6	171.1	68.5	246.7	91.7	44.6
$\Delta R_{1\to2}[Hz]$	**0.0**	**-24.8**	**-7.4**	**10.8**	**-9.0**	**0.0**
$\Delta R_{2\to1}[Hz]$	**0.0**	**126.5**	**23.9**	**202.1**	**47.1**	**0.0**

Table 5.1: The effect of the carrier frequency on the population transition rates

as $dP_2(0)/dt = R_{1\to2}$, and the carrier frequency is more than 6 GHz detuned from any transition starting in the $F = 1$ level.

The saturation (equilibrium) level of the population, on the other hand, is highly related to the carrier's intensity and detuning. For example, a near resonant 7 μw carrier beam (Δ=80 MHz), drops the saturation level to 0.26 (the saturation level "in the dark" is 0.63). The decay time τ measured in that case is 4500 μs, much shorter than the measured thermal relaxation time constant (8300 μs).

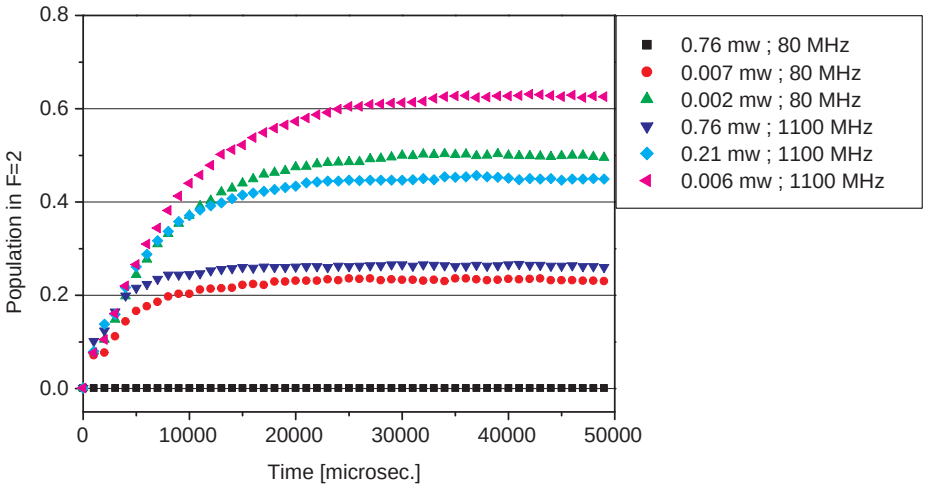

Figure 5.11: The affect of the carrier on the atomic populations is demonstrated. The different curves denote different values of laser power and detuning (see the legend).

5.3.3 The affect of non resonant excitation

Although the Raman beams are far detuned from resonance, they can still excite atomic transitions and cause scattering.. To quantify the effect of this scattering we sent each one of the Raman beams separately, to the atomic sample and monitored the evolution of P_2. The results are summarized in the table (Table 5.2) and graph (Fig. 5.12) bellow. It is obvious from these results that the pump beam's influence on the transition rates is much higher than the influence of the Stokes beam. The reason for that can be understood by looking in Fig. 5.13, wherein the relative detunings of the Raman beams from the D2 atomic transitions, $F = 1 \rightarrow F'$ and $F = 2 \rightarrow F'$, are shown. From the diagram it is clear that the affect of the pump beam on the transfer rate $R_{1\rightarrow 2}$ is much higher than that of the Stokes beam. The curve's slope at $t = 0$, which reflects the excitation rate from $F = 1$ ($R_{1\rightarrow 2}$) , will thus be much sharper for the pump beam, leading to very short coherence time of 1200μs until saturation (for a 0.76 mw beam).

properties	Stokes	Stokes	Stokes	pump	pump	pump	no light
Power[mw]	0.76	0.02	0.008	0.76	0.018	0.006	no light
A	0.365	0.54	0.635	0.45	0.522	0.63	0.63
$\tau[\mu s]$	5200	6900	8300	1200	3800	8300	8300
$R_{1\to2}[Hz]$	70.2	77.5	76.5	375.0	137.4	75.9	75.9
$R_{2\to1}[Hz]$	122.1	67.4	44.0	458.3	125.8	44.6	44.6
$\Delta R_{1\to2}[Hz]$	**-5.7**	**1.6**	**0.6**	**299.1**	**61.5**	**0.0**	**0.0**
$\Delta R_{2\to1}[Hz]$	**77.5**	**22.8**	**-0.6**	**413.8**	**81.2**	**0.0**	**0.0**

Table 5.2: The affect of the non resonant excitation on the population transition rates. The last two rows of the table (highlighted) show the net affect of non resonant excitation, after subtracting the thermal relaxation rates. results.

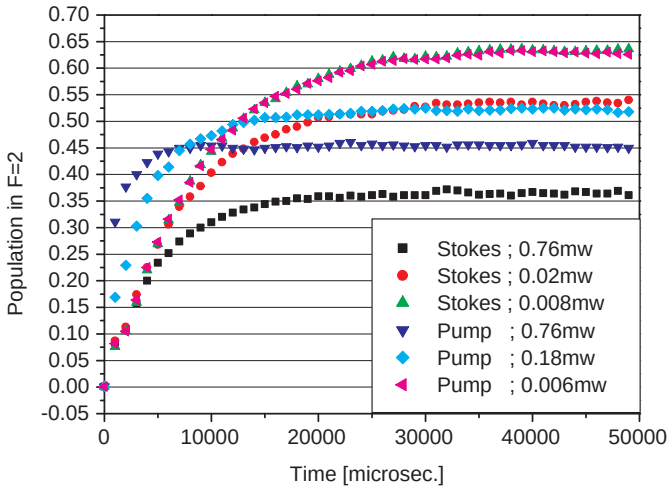

Figure 5.12: The effect of spontaneous emission induced by Raman beams on the population evolution in $F = 2$. We show results for various beam intensities.

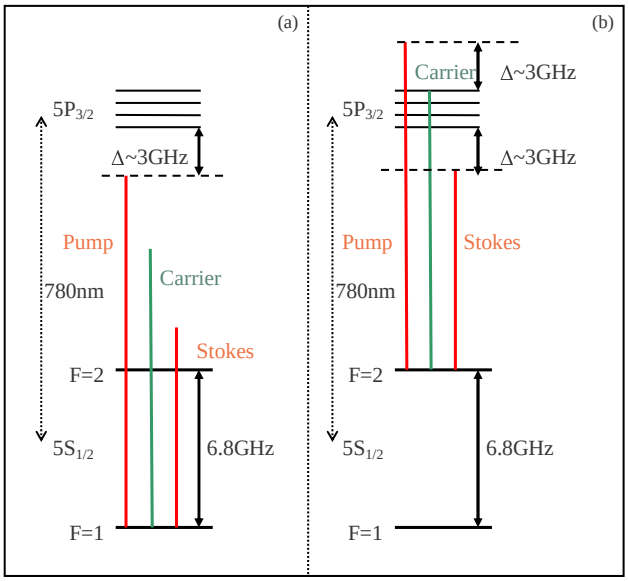

Figure 5.13: The Raman beams detuning from the excited state. (a)- the detuning from the transition $F = 1 \rightarrow F'$, (b)- the detuning from $F = 2 \rightarrow F'$ is visualized.

5.3.4 Coherent results

The total effect of noncoherent processes on the evolution of the population in $F = 2$ level is presented by the blue plot in Fig. 5.14. On the same graph we show the thermal relaxation curve (green plot), and two representative results of the interaction between the atoms and the Raman beams (black and red plots). Let us first focus our attention at shorter times (hundreds of μs). We notice that noncoherent processes alone cannot explain the population evolution in $F = 2$. For example, a 200μs Raman pulse transfers 30% of the population to the $F = 2$ level, while noncoherent processes and thermalization predict just 7% transfer.
We can therefore conclude that this rapid increase in the population of $F = 2$ is the result of coherent two-photon interaction in the system, that is, Rabi pupulation oscillations induced by the Raman laser beams.
However, as the population in $F = 2$ grows, so does the effect of the carrier beam component (as described in Sect. 5.3.2). We have found that each one of the Raman beams includes a small component in the frequency of the carrier beam (see Sect. 5.1, fig 5.5). The optical path of each beam is different and its length is subject to random fluctuations due to vibration. As a result, the two components of the carrier beam interfere randomly with each other,

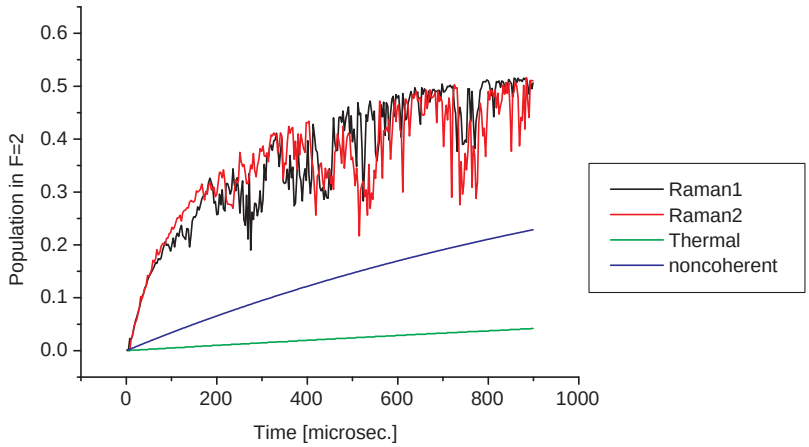

Figure 5.14: The noncoherent effects (blue plot) are shown comparing to the evolution of P_2 in the Raman field.

causing random intensity fluctuation of the carrier beam component reaching the atomic sample. It is now clear that this random intensity fluctuation of the carrier beam component will cause large and random fluctuations in the population of the $F = 2$ level, as is observed in fig 5.14 above.

We suggest that the following steps be taken as to decrease the non coherent effects:

- Mach-Zender interferometer: The filterring of the carrier frequency (which is resonant with the atomic transition) by a MZ interferometer will greatly reduce the scattering rate and the random population fluctuations in our system.

- Far detuned Raman: The ∼3 GHz detuning should be increased to fight spontaneous emission. A detuning of several tens of GHz can be achieved either by changing our locking scheme or by working with free running lasers.

- The Rabi frequency: Since we have noticed the beginning of a coherent process at early times of the interaction, we suggest the Rabi frequency will be increased, so that many cycles can be observed. We have not yet found a way to increase the Rabi frequency in our systems since we are limited by the given output power of our lasers.

Finally, we would like to mention that to the best of our knowledge, observation of Raman induced Rabi oscillations in room temperature atoms, has not yet been reported.

Chapter 6

Summary

In this work we studied ways to coherently manipulate two-state atomic systems, and realized experimentally two of these methods.

We designed and built a versatile experimental setup (detailed in Chap. 3) which can manipulate ^{87}Rb atoms through direct microwave radiation as well as through interaction with Raman laser beams. The lasers in the experiment are used both to manipulate the atoms and to probe their state. All the lasers are home made and two of them have extended cavities and are stabilized via locking to an atomic transition. These lasers have reasonable stability and sub-MHz linewidth.

All the experiments described in this thesis were done with room temperature ^{87}Rb atomic vapor. We used a buffered vapor cell (with Ne at 7.5 Torr) so as to minimize decoherence.

Our computerized detection system detects variations in the atomic population through changes in the absorption profile of a probe beam locked to an atomic transition. The evolution of the atomic population in the absence of any radiation is used for calibration.

We detected Rabi oscillations in the population, induced by microwave radiation. The measured generalized Rabi frequency is between 0.2 and 3 KHz. The typical decay time of the oscillations is around 5 ms. We estimated (with an uncertainty of 12 Hz) the hyperfine splitting frequency, based on the location of the minimum in the curve describing the dependence of the Rabi frequency on the microwave frequency. As expected, this frequency is pressure-shifted because of the interaction of the rubidium atoms with the buffer gas. In the presence of an external magnetic field, the Rabi frequency of the clock transition $|1,0\rangle \rightarrow |2,0\rangle$ is

reduced, since the other transitions are shifted by ∼0.7 MHz/G, leading to a decrease of the interaction of the atoms with the microwave radiation. We also measured the second-order shift of the clock transition with an error of less then 3% compared to the known value [Ste01].

The Raman laser system (described in Chap. 5) generates two phase-locked laser beams whose frequency difference matches the ground-state hyperfine splitting of the Rb atoms (∼ 6.8 GHz). This is achieved by modulating the injection current of our master laser diode by 3.4 GHz. The generated sidebands are then injected into two slave lasers for amplification. We monitored the beat note of the two Raman beams on a fast photodiode, and demonstrated the extremely narrow linewidth (∼1 Hz) of this beatnote signal. This narrow signal verifies that the phase difference between the beams is independent of time for at least a full second (some 3×10^{14} cycles). The Raman beams are then sent to the atomic sample.

Currently the observation of Rabi oscillations in an ensemble of room temperature atoms is not possible due to noncoherent effects (=noise). Those effects are analyzed in the last section of Chap. 5 wherein we also verify the existence of coherent effects in the system. We also propose some technical changes to the present setup. These changes will decrease the noncoherent effects so that the coherent coupling of two atomic states will be better observed.

In the future, our Raman laser system will be used to manipulate cold atoms in a magnetic trap. For this kind of experiments, the realization of Raman transitions between $\Delta m_F = 2$ states is of great relevance. These transitions are of low probability due to the relatively small hyperfine splitting of the excited state. In Sect. 2.2.4 we have given a theoretical review of this problem. We are currently exploring possible solutions.

Appendix A

The effect of the radiation phase on the Bloch vector's evolution

We have previously shown (see Sect. 2.1.3, 2.1.6) that the effect of a Rabi pulse of zero-phase near-resonant radiation on a two state system can be represented as a rotation of the Bloch vector around the x axis. To see the effect of non-zero phase, let us rewrite the TD Schrödinger equation for the probability amplitudes of the two-state system:

$$\frac{d}{dt}\begin{pmatrix} C_0(t) \\ C_1(t) \end{pmatrix} = -\frac{i}{2}\begin{pmatrix} -\delta & \Omega^* \\ \Omega & \delta \end{pmatrix}\begin{pmatrix} C_0(t) \\ C_1(t) \end{pmatrix} \tag{A-1}$$

where $\Omega = |\Omega|e^{-i(\omega t+\phi)}$. Assuming that we know the solution for ϕ=0, let us define the matrix $\hat{K}$ as

$$\hat{K} = \begin{pmatrix} 1 & 0 \\ 0 & e^{-ik} \end{pmatrix}. \tag{A-2}$$

We can easily see that $\hat{K^T}\hat{K} = I$, so that $\hat{K^T} = K^{-1}$. Also, if we look at the representation of the vector $\hat{\mathbf{D}} = \hat{K}\hat{\mathbf{C}}$ on the Bloch sphere, we will see that if $\hat{\mathbf{C}}$ is represented by a point (θ,ϕ), then D is represented by a point (θ,$\phi - k$). We can therefore conclude that $\hat{K}$ is a rotation matrix that rotates the XY plane by an angle k around the z axis. We can now replace $\hat{\mathbf{C}}$ in (A-1) by $\hat{K^T}\hat{\mathbf{D}} = \hat{\mathbf{C}}$ to get

$$\hat{K^T}\dot{\hat{\mathbf{D}}} = \hat{H}\hat{K^T}\hat{\mathbf{D}} \tag{A-3}$$

where

$$\hat{H} = -\frac{i}{2}\begin{pmatrix} -\delta & \Omega^* \\ \Omega & \delta \end{pmatrix}. \tag{A-4}$$

Multiplying both sides of the equation from the left by the matrix $\hat{K}$ and using the definition of Ω we get

$$\frac{d}{dt}\begin{pmatrix} D_0(t) \\ D_1(t) \end{pmatrix} = -\frac{i}{2}\begin{pmatrix} -\delta & |\Omega|e^{i\omega t+\phi+k} \\ |\Omega|e^{-(i\omega t+\phi+k)} & \delta \end{pmatrix}\begin{pmatrix} D_0(t) \\ D_1(t) \end{pmatrix}. \tag{A-5}$$

By choosing $k = -\phi$ this equation is reduced to equation (A-1). We know the solution of that equation, and we know that the time evolution of the solution can be represented on the Bloch sphere as a rotation around the x axis. We can thus conclude that the evolution of $\hat{\mathbf{C}} = \hat{K^T}\hat{\mathbf{D}}$ can be represented on the Bloch sphere as a rotation around an axis x', which lies on the XY plane and is rotated by an angle $-\phi$ to the x axis.

Therefore, we have shown that the effect of adding a phase ϕ to a Rabi pulse can be represented on the Bloch sphere as a rotation of the XY plane by $-\phi$.

Appendix B

Double resonance spectroscopy

In section 4.2.3 we described the Rabi oscillations induced by a near resonant microwave radiation in the presence of a constant magnetic field. In the following we explore the effect of the angle between the constant magnetic field and the magnetic component of the microwave field on the Rabi oscillations.

We use a method known as double resonance spectroscopy. This method combines both laser and microwave radiation: First, we apply a laser field tuned to the $F = 2 \rightarrow F' = 3$ transition frequency. As described in Sect. 3.4, this field pumps all the atoms to $F = 1$ level. A microwave field resonant with any one of the possible hyperfine transitions can now excite the atoms to $F = 2$ from where they are immediately excited to $F' = 3$ by the laser light. The absorption is indicated by a drop in the laser light intensity, which we monitor by a photodiode. Scanning over the microwave frequency we can obtain the Zeeman split absorption spectrum of the ground state hyperfine levels.

The possible transitions within the ground state are shown in Fig. B-1. The expected shifts of the various transitions from the hyperfine split frequency are summarized in the table attached.

In the experiment we positioned the antenna so that the magnetic field induced by the microwave radiation will oscillate in the direction of the z axis (see Fig. 4.2). We monitored the absorption spectrum for different directions of the constant field. The results are shown in Fig. B-2.

It is clear that the direction of the quantiztion axis, determined by the constant field, affects

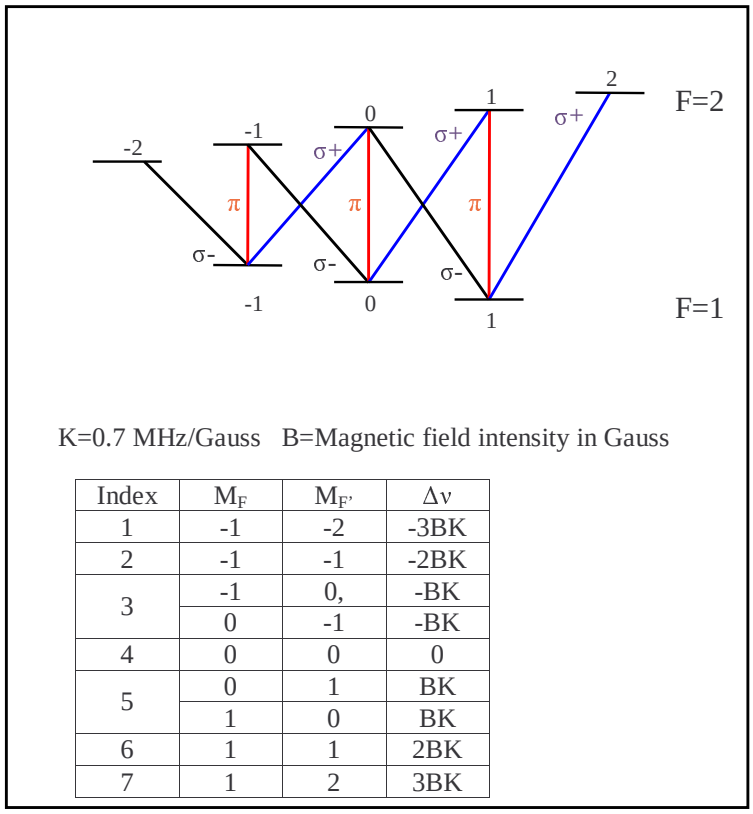

Index	M_F	$M_{F'}$	$\Delta\nu$
1	-1	-2	-3BK
2	-1	-1	-2BK
3	-1	0,	-BK
	0	-1	-BK
4	0	0	0
5	0	1	BK
	1	0	BK
6	1	1	2BK
7	1	2	3BK

Figure B-1: The diagram of the different transitions between Zeeman sublevels

the absorption spectrum. When the induced microwave magnetic field oscillates in parallel to the quantization axis, only the π transitions ($\Delta m_F = 0$) are induced. When the constant and the microwave fields are perpendicular we see only the absorption lines of the σ transitions. If the microwave field have both perpendicular and parallel components to the quantization axis, we will get the full absorption spectrum.

Thus the observation of Rabi oscilations between $m_F = 0$ states is possible only when the fields are parallel, and we verified it experimentally.

The observation of Rabi oscillations along any of the other π and σ transitions is impossible, in our setup, as small fluctuations in the magnetic fields (~ 0.01 G) lead to fluctuations of several KHz in the Zeeman shift. This noise completly covers Rabi oscillations of several KHz.

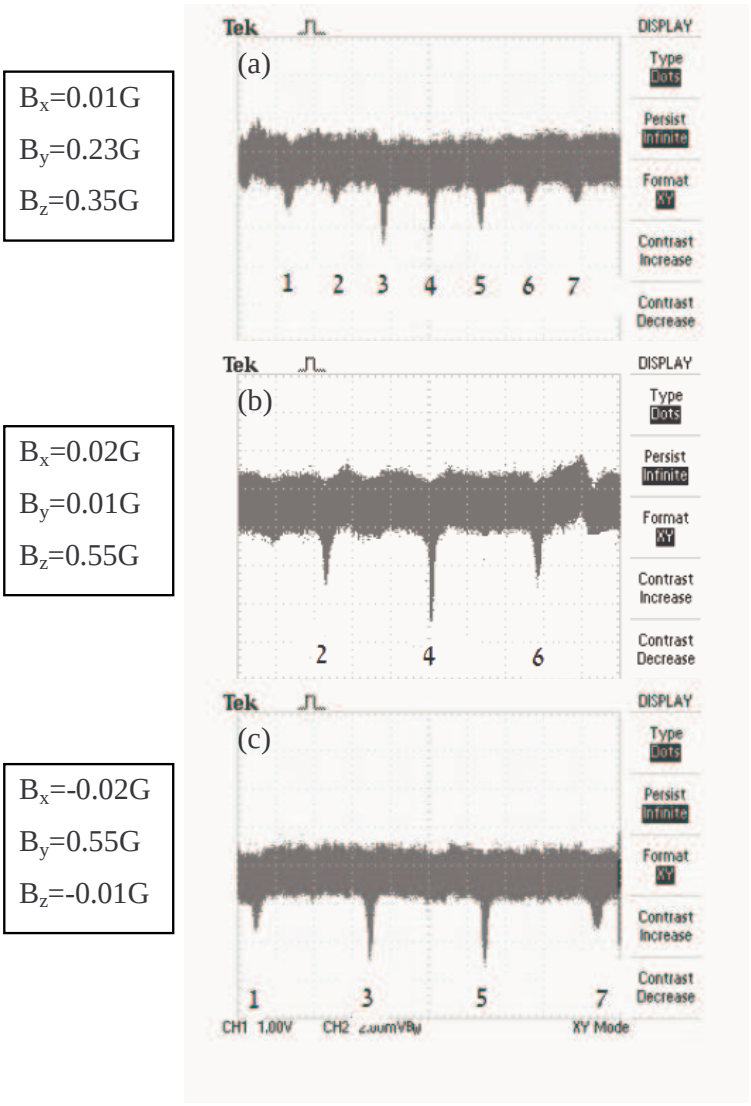

Figure B-2: The absorption spectrum of the ground state in different external fields. The various components of the DC field in the specific measurement are noted in the frame. In all measurements the microwave field oscillates at the z axis direction. The various transition lines are marked by an index number (see Fig. B-1).

Bibliography

[Bra97] S. Brandt, A. Nagel, R. Wynands, D. Meschede, *Buffer-gas-induced linewidth reduction of coherent dark resonances to below 50 Hz*, Phys. Rev. A **56**, (1997).

[Bra98] S. Brattke, U. Kallmann, W. D. Hartmann, *Coherent dark states of ^{87}Rb in a buffer gas using pulsed laser light*, Eur. Phys. J. D **3**, p. 159 (1998).

[Dem03] W. Demtröder, *Laser Spectroscopy 3rd Ed.*, Springer, (2003).

[Dic53] R. H. Dicke, *The effect of collisions upon the doppler width of spectral line*, Physical Review **89**, p. 472, (1953).

[Dot02] I. Dotsenko, *Raman spectroscopy of single atoms*, Diploma Thesis, Bonn University, (2002).

[Fru85] R. P. Frueholz, C. H. Volk, *Analysis of Dicke narrowing in wall-coated and buffer-gas-filled atomic storage cells*, Journal Physics B **18**, p. 4055, (1985).

[Giv06] M. Givon, *Walks on the Bloch sphere*, Ph.D Research Proposal, Ben Gurion University, (2006).

[Hap72] W. Happer, *Optical pumping*, Review Of Modern Physics **44**, p. 169, (1972).

[Hau00] D. Haubrich, M. Dornseifer and R. Wynands, *Lossless beam combiners for nearly equal laser frequencies*, Rev. Sci. Inst. **71**(2), p. 225, (2000).

[Jen76] F. A. Jenkins and H. E. White, *Fundamentals of optics*, McGraw-Hill, (1976).

[Kuh03] S. Kuhr, *A controlled quantum system of individual neutral atoms*, PhD. Thesis, Bonn university, (2003).

[Kin99] B. E. King, *Quantum State Engineering and Information Processing with Trapped Ions*, PhD. Thesis, Univ. of Colorado, (1999).

[Mab01] H. Mabuchi, *Physics course notes*, http://minty.caltech.edu/Ph195/courseinfo.htm, (2001).

[Met99] H. J. Metcalf and P. van der Straten, *Laser Cooling and Trapping*, (1999).

[Mue01] M. Mueller, *Ramankühlung einzelner Atome*, diplomarbeit, Universität Bonn (2001).

[Orl04] T. P. Orlando, *Superconducting Circuits and Quantum Computation*, Ch. 20 of RLE progress report, MIT, (2004).

[Pea02] C. P. Pearman et al., *Polarization Spectroscopy of a Closed Atomic Transition: Applications to Laser Frequency Locking*, J. Phys. B: At. Mol. Opt. Phys. **35**, p. 5141, (2002).

[Pet98] S. J. H. Petra, *Development of frequency stabilized laser diodes for building a Magneto-Optical Trap*, Thesis, Amsterdam University (1998).

[Ric95] L. Ricci, M. Weidemüller, T. Esslinger, A. Hemmerich, C. Zimmermann, V. Vuletic, W. König and T.W. Hänsch, Opt. Comm. **117**, p. 541, (1995).

[Rin99] J. Ringot, Y. Lecoq, J. C. Garreau and P. Szriftgiser, *Generation of phase-coherent laser beams for Raman spectroscopy and cooling by direct current modulation of a diode laser*, Eur. Phys. J. D, **65**, p. 285, (1999).

[Sho90] B. W. Shore, *The Theory of Coherent Atomic Excitation*, Wiley, New York, (1990).

[Ste01] D. A. Steck, *Rubidium 87 D Line Data*, Los Alamos National Laboratory, (2001).

[Tre06] P. Treutlein, T. Steinmetz, Y. Colombe, B. Lev, P. Hommelhoff, J. Reichel, M. Greiner, O. Mandel, A. Widera, T. Rom, I. Bloch, T. W. Hänsch, *Quantum Information Processing in Optical Lattices and Magnetic Microtraps*, Fortschr. Phys. **54**(8-10), p. 702, (2006).

[Van01] L. M. K. Vandersypen, M. Steffen, G. Breyta, C. S. Yannoni, M. H. Sherwood, I. L. Chuang, *Experimental realization of Shor's quantum factoring algorithm using nuclear magnetic resonance*, Nature **414**, p. 883, (2001).